Supporting information: Microkinetic modelling of postplasma catalysis to improve the conversion of dry reforming of methane in a gliding arc plasmatron

Sara Ceulemans^{a,b,*}, Eduardo Morais^{a,b}, Björn Loenders^{a,b}, Annemie Bogaerts^{a,b,*}

* Corresponding authors:

annemie.bogaerts@uantwerpen.be (A. Bogaerts)

sara.ceulemans@uantwerpen.be (S. Ceulemans)

S1. Model

S1.1 Chemistry

Table S1: Energies calculated with density functional theory (DFT) in Ref. [1], that are used in the surface chemistry set. All energies are given in kJ/mol and the rate coefficients are given in cm³/s. E_a is the activation energy for adsorption, corresponding to ΔH_{act} in Equation 9, which is then used in Equation 7, E_r is the reaction energy for adsorption, corresponding to $\Delta H_{ads,DFT}$ in Equation S1, and $E_{a, forward}$ and $E_{a, backward}$ are the activation energies for the forward and backward surface reactions, respectively, also corresponding to ΔH_{act} in Equation 9, which is then used in Equation 6. These equations are outlined in the paper. The values in this table account for the corrections for CO* overbinding and H* destabilisation.

Reaction ^a	Energy (kJ/mol)	Ni(111)	Ni(110)	Ni(100)	Ni(211)
$CH_4(g) + fs^* + fs^* \rightleftharpoons CH_3^* + H^*$	Ea	130	99	112	117
$CH_4(g) + js + js \leftarrow CH_3 + H$	$\mathrm{E_{r}}$	53	49	55	24
$CO_{\bullet}(s) + fs^* \rightarrow CO_{\bullet}^*$	E_a	49	17	29	2
$CO_2(g) + fs^* \rightleftharpoons CO_2^*$	$E_{\rm r}$	25	-42	-16	-39
$H_2O(g) + fs^* \rightleftharpoons H_2O^*$	E_a	0	0	0	0
	$E_{\rm r}$	-22	-38	-31	-48
$II (a) + fa^* + fa^* \rightarrow II^* + II^*$	E_a	0	2	0	0
$H_2(g) + fs^* + fs^* \rightleftharpoons H^* + H^*$	$E_{\rm r}$	-57	-37	-64	-62
$CO(s) + fs^* \rightarrow CO^*$	E_a	0	0	0	0
$CO(g) + fs^* \rightleftharpoons CO^*$	$E_{\rm r}$	-138.6	-134.5	-134.8	-146.7
$CH_3^* + fs^* \rightleftharpoons CH_2^* + H^*$	E _{a, forward}	53	55	76	59
	Ea, backward	39	16	106	34
$CH_2^* + fs^* \rightleftharpoons CH^* + H^*$	E _{a, forward}	21	27	0	26
	Ea, backward	40	48	50	64
	E _{a, forward}	108	76	38	38

^{a.} Research group PLASMANT and Center of Excellence PLASMA, Department of Chemistry, University of Antwerp, Groenenborgerlaan 171, 2020 Antwerp, Belgium

^{b.} Electrification Institute, University of Antwerp, Olieweg 97, 2020 Antwerp, Belgium

CII* + £-* > C* + II*	Б	<i>5</i> 1	(0	5.4	52
$CH^* + fs^* \rightleftharpoons C^* + H^*$	E _{a, backward}	51	60	54	52
$CO_2^* + fs^* \rightleftharpoons CO^* + O^*$	E _{a, forward}	50	39	15	91
2 ,	Ea, backward	134	37	86	138
$CO_2^* + H^* \rightleftharpoons COOH^* + fs^*$	E _{a, forward}	56	78	78	80
	E _{a, backward}	63	66	64	67
$CO_2^* + H^* \rightleftharpoons HCOO^* + fs^*$	E _{a, forward}	42	15	35	77
2	E _{a, backward}	85	53	63	118
$HCOO^* + fs^* \rightleftharpoons CHO^* + O^*$	E _{a, forward}	136	134	158	167
11000 1 75 (0110 1 0	E _{a, backward}	99	69	188	133
$COOH^* + fs^* \rightleftharpoons CO^* + OH^*$	$E_{a, forward}$	29	34	30	37
00011 1 / 3 (00 1 011	E _{a, backward}	95	92	94	115
$CH_3^* + OH^* \rightleftharpoons CH_3OH^* + fs^*$	E _{a, forward}	237	257	236	274
Uli3 1 Uli ← Uli3Uli 1 J 3	Ea, backward	166	156	151	147
$CH_3OH^* + fs^* \rightleftharpoons CH_2OH^* + H^*$	E _{a, forward}	75	68	66	59
CH30H + J3 ~ CH20H + H	E _{a, backward}	58	51	61	69
$CH_2^* + OH^* \rightleftharpoons CH_2OH^* + fs^*$	E _{a, forward}	131	148	143	228
$CH_2 + OH \leftarrow CH_2OH + JS$	Ea, backward	57	68	24	136
$CH \cap U^* + f_{\sigma^*} \rightarrow CH \cap U^* + U^*$	E _{a, forward}	48	11	30	20
$CH_2OH^* + fs^* \rightleftharpoons CHOH^* + H^*$	Ea, backward	51	23	34	23
CU* OU* > CUOU* f-*	E _{a, forward}	154	155	184	240
$CH^* + OH^* \rightleftharpoons CHOH^* + fs^*$	Ea, backward	63	66	20	112
	E _{a, forward}	0	79	15	43
$CHOH^* + fs^* \rightleftharpoons COH^* + H^*$	Ea, backward	84	71	121	87
	E _{a, forward}	132	141	162	188
$C^* + OH^* \rightleftharpoons COH^* + fs^*$	E _{a, backward}	180	61	88	90
	E _{a, forward}	76	32	85	31
$COH^* + fs^* \rightleftharpoons CO^* + H^*$	E _{a, backward}	121	94	92	81
	E _{a, forward}	173	198	168	253
$CH_3^* + O^* \rightleftharpoons CH_3O^* + fs^*$	E _{a, backward}	114	182	115	198
	E _{a, forward}	100	99	54	106
$CH_3O^* + fs^* \rightleftharpoons CH_2O^* + H^*$	E _{a, backward}	79	91	72	68
	E _{a, forward}	140	68	174	188
$CH_2^* + O^* \rightleftharpoons CH_2O^* + fs^*$	E _{a, backward}	73	82	109	120
	Ea, forward	15	29	21	29
$CH_2O^* + fs^* \rightleftharpoons CHO^* + H^*$	Ea, backward	47	25	48	77
	Ea, forward	144	109	250	225
$CH^* + O^* \rightleftharpoons CHO^* + fs^*$	E _{a, backward}	89	98	162	167
	E _{a, forward}	20	31	68	2
$CHO^* + fs^* \rightleftharpoons CO^* + H^*$	E _{a, backward}	98	57	82	43
	E _{a, backward}	153	99	209	168
$C^* + O^* \rightleftharpoons CO^* + fs^*$	E _{a, backward}	234	130	118	138
		69	50	36	39
$CH_3OH^* + fs^* \rightleftharpoons CH_3O^* + H^*$	E _{a, forward}	91	87	90	94
	E _{a, backward}	38	87	51	57
$CH_2OH^* + fs^* \rightleftharpoons CH_2O^* + H^*$	E _{a, forward}	56	132	127	64
	E _{a, backward}	46	25	43	117
$CHOH^* + fs^* \rightleftharpoons CHO^* + H^*$	E _{a, forward}	94	54	142	169
	E _{a, backward}	94	88	142	
$O^* + H^* \rightleftharpoons OH^* + fs^*$	E _{a, forward}				78
-	Ea, backward	86	137	119	96
$OH^* + H^* \rightleftharpoons H_2O^* + fs^*$	E _{a, forward}	99	131	119	125
	E _{a, backward}	72	96	75	72
$OH^* + OH^* \rightleftharpoons H_2O^* + O^*$	E _{a, forward}	62	110	73	106
	Ea, backward	46	27	51	35

$COOH^* + * \rightleftharpoons COH^* + O^*$	Ea, forward	112	223	120	165
COOH + * ≠ COH + O	Ea, backward	144	171	200	175
Reaction ^b	k (same for all facets)				
$CO(g) + CO^* \rightleftharpoons CO_2(g) + C^*$	$k_{ m forward}$	k_{forward}			$\frac{1000}{N_A}$
	k _{backward}	9.07 ×		<u>-24346.6</u>	$<\frac{1000}{N_A}$

- a) fs* indicates a free site on the catalyst surface
- b) Rate coefficients taken from [2]

S1.2 Corrections on enthalpy input

In contrast to the activation enthalpy in Equation 9 in the main paper, the adsorption enthalpy from Equation 10 is not directly taken from Ref. [1], but has been adjusted to take some corrections into account regarding the gas-phase species. In this way, our enthalpy values become [3]:

$$\Delta H_{ads} = H_{surf} - H_{gas} = H_{surf} - (H_{gas,DFT} + H_{corr}) = (H_{surf} - H_{gas,DFT}) - H_{corr}$$

$$= \Delta H_{ads,DFT} - H_{corr}$$
(S1)

$$H_{corr} = N_A \left(H_{ZPE} + C_p T_{gas} + \sum_i \frac{\nu_i}{e^{\nu_i/k_B T_{gas}} - 1} \right)$$
 (S2)

$$H_{ZPE} = \frac{1}{2} \sum_{i} \nu_i \tag{S3}$$

$$C_p = k_B + \frac{3}{2}k_B + k_B$$
 for linear molecules (S4)

$$C_p = k_B + \frac{3}{2}k_B + \frac{3}{2}k_B \text{ for nonlinear molecules}$$
 (S5)

With H_{surf} and H_{gas} being the enthalpy of the same species adsorbed on the surface and in the gas phase, respectively, $H_{gas,DFT}$ the enthalpy of the gas-phase species calculated from DFT, H_{corr} the corrections on the enthalpy of this species in the gas phase, N_A Avogadro's constant, H_{ZPE} the zero-point energy (ZPE) of this gas species, C_p the heat capacity at constant pressure, and v_i a frequency of this gas-phase species, with the sum being taken over all frequencies of the species. $\Delta H_{ads,DFT}$ is the reaction enthalpy mentioned above that can be calculated from the DFT values in Ref. [1], given in Table S1. The zero-point energy H_{ZPE} is calculated from the vibrations given in Table S2, which were taken from Ref. [4]. In these equations, we only included the ZPE for the gas-phase species, not for the surface species, because the frequency data were not available for these calculations.

Another correction made to the enthalpy, which was already added in Equation 10, is the lateral interaction energy E_{lat} . It causes a decrease in desorption activation energy, and therefore an increase in adsorption reaction energy, and is based on Ref. [1] and Ref. [5]. It is defined as:

$$E_{lat}^{atom} = E_{\theta_{lat}=1}^{atom} \frac{\left(101^{\theta_{lat}} - 1\right)}{100}$$
 (S6)

$$\theta_{lat} = \frac{(1 - \theta_* - 0.5 \times \theta_{H^*}) - \theta_{LB}}{\theta_{UB} - \theta_{LB}} \text{ with } \theta_{lat} \ge 0$$
 (S7)

With E_{lat}^{atom} being the lateral interaction energy of a certain atom, in this case either C, O or H, $E_{\theta_{lat}=1}^{atom}$ the lateral interaction energy when θ_{lat} is equal to 1 $(E_{\theta_{lat}=1}^C = E_{\theta_{lat}=1}^O = 60 \text{ kJ/mol} \text{ and } E_{\theta_{lat}=1}^H = 60 \text{ kJ/mol}$ 15 kJ/mol), θ_{lat} the (adjusted) total coverage, θ_* and θ_{H^*} the fraction of the free sites and the coverage of H*, respectively, and θ_{LB} and θ_{UB} the lower and upper boundary, which we set to 0.25 and 0.75 respectively, similar to Ref. [1] and Ref. [5]. The total coverage θ_{lat} is equal to the sum over all the surface species coverages, which can also be calculated as the total fraction (= 1) minus the fraction of free sites, with as exception H*, of which only half the coverage is used, because H* is a small species and will influence the lateral interaction to a lower extent. The lateral interaction energy of a certain surface species is then calculated as the sum of the lateral interaction energies of its constituent atoms, e.g. for CO₂, $E_{lat}^{CO_2} = E_{lat}^C + 2E_{lat}^O$. As mentioned in the references from which we took these formulas, this adds the effect of the lateral interaction in a qualitative, but not quantitative, way. In Ref. [1], the use of the same lateral interaction energy parameters at $\theta_{lat} = 1$ compared to Ref. [5], changing from Co to Ni, has been justified by the small difference in electronegativities between the two metals, as well as a sensitivity analysis on the values of these lateral interaction energies at $\theta_{lat} = 1$. Because we use a different reactant gas mixture compared to CO₂/H₂ in Ref. [1], a similar sensitivity analysis was carried out and presented in Section S2.1.4 below.

S1.3 Entropy calculation details

In Equation 11 in the main paper, the entropy has been divided over a translational and a rotational entropy, which are calculated as follows [3]:

$$S_{trans} = R \left\{ ln \left[\left(\frac{2\pi m k_B T_{gas}}{h^2} \right)^{\frac{3}{2}} \frac{k_B T_{gas}}{p_{ref}} \right] + \frac{5}{2} \right\}$$
 (S8)

$$S_{rot} = R \left[ln \left(\frac{8\pi^2 I k_B T_{gas}}{\sigma h^2} \right) + 1 \right]$$
 for linear molecules (S9)

$$S_{rot} = R \left\{ ln \left[\frac{\sqrt{\pi I}}{\sigma} \left(\frac{8\pi^2 k_B T_{gas}}{h^2} \right)^{3/2} \right] + \frac{3}{2} \right\} for nonlinear molecules$$
 (S10)

With I being the moment of inertia in kg m² for linear molecules and the product of the three moments of inertia in kg³ m⁶ for nonlinear molecules and σ the symmetry number of the molecule. The molecular

masses, moments of inertia and symmetry numbers for the gas species included in the model are given in Table S2 [6,7].

Table S2: Input parameters used to calculate the enthalpy and entropy of the gas-phase species. The molecular mass is also used in the calculation of the rate coefficient of adsorption reactions. The vibrations must be converted to J before they can be used in Equations S2 and S3.

Casamasias	Molecular mass	Moment of inertia	Symmetry number	Vibrations
Gas species	(kg)	$(kg m^2 or kg^3 m^6)$	(/)	(cm ⁻¹)
CH ₄	2.6638×10 ⁻²⁶	1.5235×10 ⁻¹³⁹	12	2917.0, 1534.0 (×2), 3019.0 (×3), 1306.0 (×3)
CO ₂	7.3080×10 ⁻²⁶	7.1738×10 ⁻⁴⁶	2	1333.0, 2349.0, 667.0 (×2)
H ₂ O	2.9916×10 ⁻²⁶	5.8396×10 ⁻¹⁴¹	2	3657.0, 1595.0, 3756.0
H ₂	3.3476×10 ⁻²⁷	4.6001×10 ⁻⁴⁸	2	4401.2
СО	4.6512×10 ⁻²⁶	1.4560×10 ⁻⁴⁶	1	2169.8

In the calculation of the Gibbs free energies, some assumptions are made that will be addressed here. Firstly, we assume that for the surface reactions and adsorption reactions, the Gibbs free activation energy is equal to the enthalpy, with no entropy included. In general, we did not include entropy for the surface species, as they require the vibrations of the surface species, which were not included in the paper from which we took the enthalpy values, and using the values from another paper would lead to an inconsistent chemistry set. A more elaborate justification is given in Section 2.1.1 in the main paper. For the adsorption reactions, the entropic contribution is already included in the first factor of the Hertz-Knudsen equation, as can be seen in the derivation given in Ref. [8], and therefore, no simplification was needed. Secondly, we assumed that the entropy of the gas species consists only of the translational and rotational entropy, without including the vibrational entropy. We decided to leave this out to limit the complexity of our model, and because we also do not include the vibrational entropy of the surface species, but we estimated from the NIST CCCBDB database the contribution of vibrational entropy to the total entropy and found that for our conditions, the contribution to the total entropy remains around 10 % or lower [6]. More specifically, at 800 K and 1000 K, the vibrational contributions range from 0.02 % to 7.1 % and from 0.07 % to 8.8 %, respectively. Given the intrinsic approximations of a 0D modelling

framework, these low contributions justify our approach to not include the gas-phase vibrational entropies.

S1.4 Solver settings

As mentioned in the main paper, the set of differential equations is solved in Python using the solve_ivp function in the scipy.integrate module. This solver requires several settings, which are discussed here. First, a method for the integration must be chosen, which in our case is the Backward Differentiation Formula (BDF), as it is an implicit method used for stiff differential equations, such as in our model. The tolerances are set to 10^{-30} for the absolute tolerance and 10^{-5} or 10^{-6} for the relative tolerance. For the GAP simulations, a relative tolerance of 10^{-6} is used to resolve the net adsorption or desorption rates, which are much lower than the absolute adsorption and desorption rates. For the validation simulations, a relative tolerance of 10^{-5} was sufficient. In addition, the numerical precision is equal to a default double precision of 64 bits (i.e., IEEE 754 double precision), which was tested to be sufficient for our simulations as well.

Additionally, it should be mentioned that while the time-stepping in solve_ivp is done automatically, we do not set the end time of the solve_ivp function immediately equal to the end time of our simulation (3600 s or 10 000 s), which would lead to solve_ivp being applied only once. Instead, two time-stepping mechanisms are present: automatic time-stepping integrated in the solve_ivp function and an overarching manual time-stepping equation, which was included for model stability. In this way, the total calculation time is divided into manually determined shorter timesteps, especially at the start of the simulation, and for each of these timesteps the solve_ivp function solves the differential equations. This timestep is calculated using the equation $\Delta t = \Delta t_{-1} \times 10^s$, with Δt being the new timestep, Δt_{-1} the previous timestep and s an exponent, which can be varied to make the increase in timestep shorter or longer. The first timestep has a value of 10^{-12} s, and each subsequent timestep will be calculated with the formula above. In general, an s-value of 1 is applied.

S1.5 Model validation

For the model validation, two studies describing results for (among other results) thermal catalysis are used. We compare these thermal catalysis results to our modelling simulations, for which we made two adjustments: (i) we assume that the complete reactor corresponds to one CSTR. This includes a gas flow in and out of the reactor, a catalyst packing and perfect mixing throughout the complete reactor; and (ii) we also did not include any gas-phase reactions in these simulations, only the surface reactions were included and validated. There are two reasons for this second assumption. First, the gas-phase chemistry set was taken from Ref. [9] and was already validated in that work. Leaving out the charged species will

not influence the validation, because as mentioned in the main paper, the conversion can be assumed thermal for our conditions. Second, at the temperatures used in the experiments, test simulation results with our model indicate that thermal gas conversion is too slow to significantly change the results and can be neglected below 1200-1300 K for Paper 1 and at least 1500 K for Paper 2 (under the same conditions of the two validation papers). Because the temperature ranges used in these papers reach only up to 900 K and 1200 K for Paper 1 and Paper 2, respectively, we can leave out the gas-phase reactions in these calculations to reduce the calculation time. The assumptions above are made for all validation simulations. In the sections below, we describe the input parameters for the two papers separately.

This paper reports results for both thermal and plasma experiments. In our case, we used the thermal catalysis results, for DRM only. The gas temperature is varied between 380 K and 900 K with steps of 52 K, and increased up to 1500 K (for the simulations only) in steps of 50 K. The flow rate of $0.3333 \, cm^3 s^{-1}$ (298.15 K and 1 atm) and the gas volume of $1.072 \, cm^3 \times 0.75 = 0.8040 \, cm^3$ are taken from the paper. The gas volume is multiplied by 0.75 because only 25 % of the discharge zone was occupied by the catalyst, as mentioned in the paper. The gas composition of the inflow and at the start of the simulation is $1/1 \, \text{CO}_2/\text{CH}_4$. However, in the experiments, helium was added to the gas mixture in the ratio $\text{CH}_4/\text{He}/\text{CO}_2$ equal to 1/2/1. To account for this, the atmospheric pressure used in the experiments was reduced by half to 0.506625 bar in the simulations. In this way, the residence time of CO_2 and CH_4 corresponds to the residence time in the experiments, and the surface reaction rates are not influenced by this total pressure (the partial pressures of CH_4 and CO_2 remain the same). The default site density of $10^{19} \, \text{cm}^{-3}$ was used in this case as well, and the simulation was run for 3600 s. At this time point, the metrics plotted for the validation did not show any significant variations.

In this paper, not only DRM is reported, but also steam reforming of methane (SRM, CH₄ + H₂O to CO + H₂), and DRM with addition of H₂ or H₂O, which we also tested, and the results for these gas mixtures are reported in this SI in Section S2.1.2, not in the main paper. Most settings were adopted from the experimental description, similar to Paper 1. The feed flow rate is equal to $67.55 cm^3 s^{-1}$ (298.15 K and recalculated from 1 atm to 1 bar) and the gas volume is $2.121 cm^3 \times 0.5 = 1.0605 cm^3$. Because the volume occupied by the catalyst is not mentioned here, we assume that it takes up half of the reactor volume, a fraction that was also used in a previous model [4]. The gas composition in this case is varied, based on the different gas mixtures used in the experiments. Recalculating their input flow rates to gas fractions, we obtain $0.5/0.5 \text{ CO}_2/\text{CH}_4$ for DRM, $0.556/0.444 \text{ H}_2\text{O}/\text{CH}_4$ for SRM, $0.378/0.295/0.327 \text{ CO}_2/\text{CH}_4/\text{H}_2$ for DRM + H₂ and $0.359/0.282/0.359 \text{ CO}_2/\text{CH}_4/\text{H}_2\text{O}$ for DRM + H₂O. Similar to Paper 1, N₂ was added to the gas mixture to dilute the reactants, and this was taken into account by lowering the pressure. As a result, the pressure of 1 bar was multiplied by the fraction of the reactant gases in the total

gas mixture (the previous gas fractions were calculated neglecting N_2), namely 0.04 for DRM, 0.036 for SRM, 0.055 for DRM + H_2 and 0.0593 for DRM + H_2 O. For this paper, we increased the site density to 4×10^{20} cm⁻³. This is in the same order of magnitude as the site density of 1.58×10^{20} cm⁻³ that is used in the model presented in Paper 2. In our case, we compare our modelling results to the experimental results presented in this paper, not their modelling results. In experiments, the results depend on how the catalyst was prepared, and together with the differences between our model and the model presented in Paper 2, and the included reactions/reaction rates in both models, this can explain the difference in site density necessary to find results that compare best with the experiments. The end time was chosen for the same reason as in Paper 1, and was equal to 3600 s for all simulations.

S1.6 Parameter variation

In this section, we discuss the implementation of the different parameter variations in more detail.

S1.6.1 Site density

The site density determines the importance of the surface reactions. Increasing the site density means there are more sites present in the same volume of reactor, on which more surface reactions can happen. As mentioned in Section 2.1.1 in the main paper, we use a default site density value of 10^{19} cm⁻³, which lies in between the site density used in Ref. [4] $(7.5\times10^{17}$ cm⁻³) and Ref. [11] $(1.58\times10^{20}$ cm⁻³). As is clear from the very large difference in site density between these two references, this is not a very clearly defined parameter and not straightforward to estimate. Therefore, to analyse the effect of our estimation and its influence on the results, we vary the site density between 10^{16} cm⁻³ and 10^{20} cm⁻³ with a factor of 10 as step size.

S1.6.2 Gas temperature in the catalyst bed

Eight temperature profiles are used in the afterglow (before the catalyst bed), that are all based on the same temperature profile of Ref. [2] and are all shown in Fig. 1b in the main paper. To obtain these temperature profiles, we start from the original temperature profile in this paper and fix the y-values (the temperatures), while the original x-values (the distances into the afterglow) are multiplied by different factors, namely by 0.2, 0.25, 0.3333, 0.5, 0.625, 0.7143, 0.8333 (the default temperature profile) and 1.0 (the original temperature profile). In this way, by keeping the temperature values constant and decreasing the distances at which these temperatures are reached, the same temperature will be reached at an earlier position after the plasma, effectively making the temperature profile more steep. As a result, at the distance where the catalyst bed starts, i.e. 5 mm, the temperature will be lower for these shortened, steeper temperature profiles, leading to a lower temperature in the catalyst bed. To compare, for the original temperature profile, the same temperature is reached at a longer distance. Therefore, a lower temperature in the catalyst bed due to a steeper temperature profile can also be correlated to a further position of the catalyst bed. A multiplication by a factor of 0.2, 0.25, 0.3333, 0.5, 0.625, 0.7143, 0.8333

and 1.0 leads to a gas temperature in the catalyst bed of 741, 779, 827, 903, 963, 1010, 1075 and 1170 K, respectively. We chose the temperature profile corresponding to 1075 K as the default one instead of the original temperature profile from Ref. [2] because it leads to a lower, more realistic gas temperature in the catalyst bed. This is also the reason why we did not elongate the temperature profile (i.e. multiplying the original distances by a factor larger than 1): this would lead to unrealistically high catalyst bed temperatures, at which the catalyst experimentally might start to degrade or sinter. The eight temperature profiles are shown in Fig. 1b, with the default and literature profiles indicated in red and blue, respectively.

S1.6.3 Plasma fraction

In Section 2.2.2 of the main paper, we explain how we accounted for the fact that not all gas is converted by the plasma, because only part of the gas passes through the plasma arc, and some of the conversion products recombine again, leading to a lower net plasma conversion. We define this as the "plasma fraction". A default plasma fraction of 25 % was estimated, but we varied the plasma fraction between 5 % and 45 % (in steps of 10 %pt.), which is the typical range of conversion in GA reactors, according to Fig. 5 in Ref. [12].

S1.6.4 Input gas mixture

We varied the initial CO₂/CH₄ ratio at the inlet, using the stoichiometric ratio of 50/50 as the default value and changing this to 10/90, 30/70, 70/30 and 90/10, similar to the ratios used in Ref. [9], and an extra ratio of 20/80. This input gas mixture is inserted into the plasma (first CSTR) and affects the plasma output, which will then go to the next CSTR, and change the output there, and so on, and in the end also changing the effect of the catalyst.

S1.6.5 Position of the catalyst bed

As a default position, the catalyst is placed 5 mm after the plasma. We changed this value to 6, 7, 8, 10, 15, 20 and 25 mm. Because we here use the original temperature profile from literature (the blue curve in Fig. 1b, not the default temperature profile), this will lead to an increase or decrease in the gas temperature in the catalyst bed, which could lead to similar results as when we change the temperature profile. However, changing the temperature profile or changing the position of the catalyst leads to different residence times in the CSTRs, and a steeper or less steep decrease in temperature in the afterglow, which may influence the results. Therefore, we chose our distances, and multiplication factors for the temperature profile, such that they give the same gas temperature in the catalyst bed, and the positions mentioned above correspond in reverse order to the catalyst bed temperatures given in Section S1.6.2 when varying the temperature. In this way, we can investigate the potential effects of the residence time and steepness of the temperature profile, or whether the gas temperature in the catalyst bed is indeed the determining factor when changing the catalyst position. As we found that the latter is more important,

the results of both parameter variations are quite similar and these results for varying position will not be discussed in the main paper, but only in this SI, in Section S2.2.1.

S1.6.6 Residence time in the plasma

The residence time in the plasma is also estimated as input in our model. As mentioned in Section 2.2.2 in the main paper, we chose a default value of 1 ms based on literature. However, to analyse the effect of this estimation on the results, we also tested a residence time of 0.01 ms, 0.1 ms, 10 ms and 100 ms. This is included in the model by changing the length of the reactor, i.e., the diameter and therefore the surface cross section area of the reactor remains the same, but length of the plasma part of the reactor is decreased or increased with a factor of 0.01, 0.1, 10 and 100, respectively. This yields CSTR volumes between 1.83×10^{-2} cm³ and 1.83×10^{2} cm³. Although the plasma CSTR is changed, the other CSTR calculations remain the same, but are influenced through the changed output from the plasma CSTR, which is used as input in the subsequent CSTR, which supplies the input for the next CSTR, and so on, in the end affecting the complete series of CSTRs that make up the reactor.

S2. Results and Discussion

S2.1 Model validation

S2.1.1 Paper 1

The CO₂ conversion and CO yield in Fig. S1 show a similar behaviour with respect to temperature as the CH₄ conversion and H₂ yield, plotted in Fig. 2 of the main paper. The modelled results correspond well to the conversion and yield based on the shifted chemical equilibrium composition, while the experimental values are slightly higher. This could be explained by the presence of some carbon deposition (which is not discussed in Paper 1) because the formation of solid carbon is not included in the chemical equilibrium calculation. Another reason for the deviation in the H₂ yield in the main paper might be that H₂ production has not yet reached the chemical equilibrium composition in the set residence time of the experiments. Also, there is a shift to higher temperatures in the model compared to the experiments, explained by the deviation in reaction enthalpy for DRM, but overall the trends for the experimental results and the modelling results are similar.

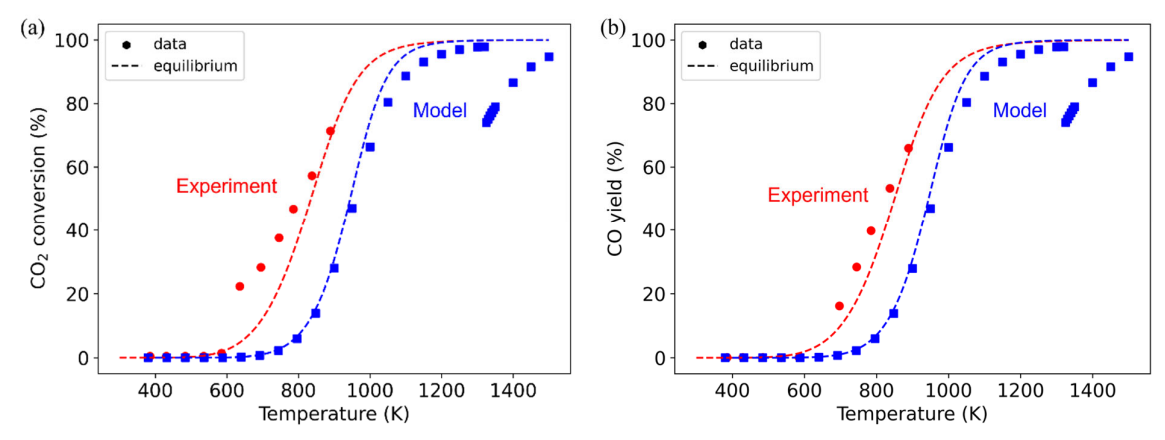


Figure S1: (a) CO_2 conversion and (b) CO yield as a function of temperature for the experiments in Ref. [10] (red circles), the modelling results (blue squares) and the corresponding chemical equilibrium values for the experiments and modelling results (red and blue dashed lines, respectively). A finer temperature interval of 5 K is used around the transition point between 1300 K and 1350 K to rule out numerical artefacts in the model.

In the main paper, the effect of C*-poisoning on the results has already been highlighted. The source of this decrease in conversions and yields is evaluated through a coverage and rate analysis, which is discussed together with the results of Paper 2 in Section 2.1.2(b) of the SI. However, a second, paper-specific analysis is discussed here. To evaluate the effect of C*-poisoning in the simulations, we carried out an analysis based on Ref. [13]. In this paper, two possible reactions for C* formation are considered, namely CH₄ decomposition (Reaction S R.1) and CO disproportionation, i.e., the Boudouard reaction (Reaction S R.2).

$$CH_4 \rightleftharpoons C^* + 2H_2 \tag{S R. 1}$$

$$2CO \rightleftharpoons C^* + CO_2 \tag{S R. 2}$$

To determine which reaction is responsible for (most of the) C^* formation and at which temperatures, two parameters α and β , similar to the reaction quotients for Reactions S R.1 and S R.2, respectively, are defined and compared to the equilibrium constants of these reactions (see Fig. S2). The definitions of α and β according to Ref. [13] are:

$$\alpha = \frac{p_{H_2}^2}{p_{CH_4}^2} \frac{1}{P_0} \tag{S11}$$

$$\beta = \frac{p_{CO_2}}{p_{CO}^2} P_0 \tag{S12}$$

Where p_{H_2} , p_{CH_4} , p_{CO_2} and p_{CO} are the partial pressures of H₂, CH₄, CO₂ and CO, respectively, and P_0 is the standard pressure of 1.0×10⁵ Pa, used to make α and β unitless. These parameters can be calculated with the results from the simulations, multiplying the output molar gas fractions by the total pressure in the reactor. The equilibrium constant K_i of reaction i (reaction S R.1 or S R.2) is calculated with:

$$K_i = e^{\left(\frac{-\Delta G_i^0}{RT_{gas}}\right)} \tag{S13}$$

With ΔG_i^0 being the Gibbs free energy of reaction i, R the gas constant and T_{gas} the gas temperature. The Gibbs free energies for the two C*-forming reactions are temperature dependent, but still following Ref. [13] they can be calculated with these formulas:

$$\Delta G_1^0 = 58886.79 + 270.55 \times T_{gas} + 0.0311 \times T_{gas}^2 - (3.00 \times 10^{-6}) \times T_{gas}^3 + \frac{291405.7}{T_{gas}} - 54.598 \times T_{gas} \times ln(T_{gas})$$
(S14)

$$\Delta G_2^0 = -188030.19 + 402.82 \times T_{gas} - 0.00542 \times T_{gas}^2 + \frac{828509.9}{T_{gas}} - 32.026 \times T_{gas} \times ln(T_{gas})$$
(S15)

With ΔG_1^0 being the Gibbs free energy for CH₄ decomposition (Reaction S R.1) and ΔG_2^0 the Gibbs free energy for CO disproportionation (Reaction S R.2), respectively, which are then inserted in Equation S13 to obtain the equilibrium constants.

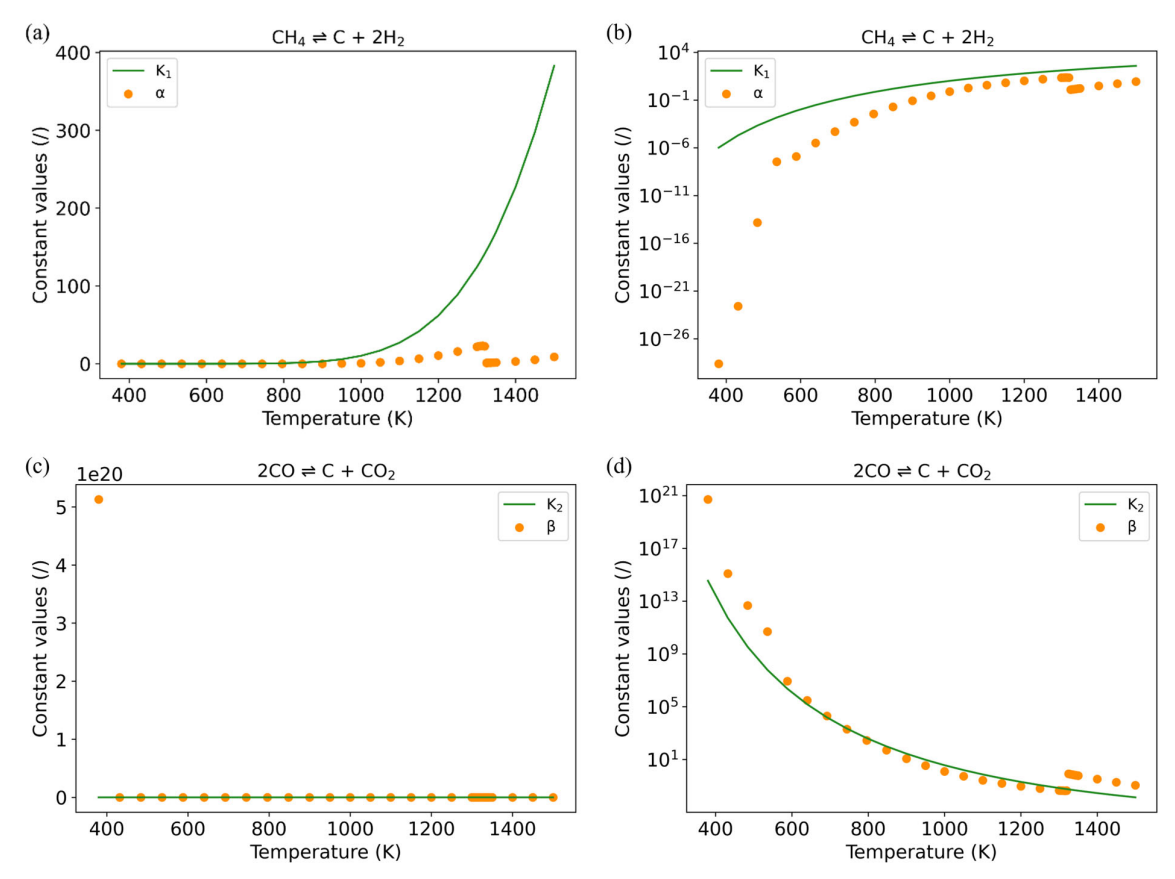


Figure S2: (a, b) α -parameter and corresponding equilibrium constant values as a function of temperature for CH₄ decomposition, both with (a) linear and (b) logarithmic y-scale. (c, d) β -parameter and corresponding equilibrium constant values as a function of temperature for CO disproportionation, both with (c) linear and (d) logarithmic y-scale for Paper 1. When the equilibrium constant values (green lines) are higher than the parameter values (orange dots) the reaction towards the right-hand side of reactions S R.1 and S R.2 will be promoted, causing carbon deposition. A finer temperature interval of 5 K is used around the transition point between 1300 K and 1350 K to rule out numerical artefacts in the model.

Fig. S2 shows a comparison of the α - and β -parameter with their respective equilibrium constants for CH₄ decomposition and CO disproportionation. When the α - or β -parameter is lower than the equilibrium constant value, less C* and H₂/CO₂ are formed compared to the amount the chemical equilibrium composition allows at that temperature, and therefore the reactants will react towards the right-hand side of reactions S R.1 and S R.2, leading to more C* formation. In this way, we can determine which reaction is responsible for the C*-poisoning visible in Fig. 2 and Fig. S1. We show the figures both with a linear y-scale and a logarithmic y-scale for clarity.

As can be seen in Fig. S2, at temperatures of 1325 K and above, only α is lower than the equilibrium constant, while β lies above the green curve. Because at these temperatures C*-poisoning is causing a decrease in conversions and yields, we can conclude from these graphs that this C*-poisoning is caused by the decomposition of CH₄. The green equilibrium constant curve in Fig. S2a clearly shows the increase in the equilibrium constant with increasing temperature, which causes an increasing difference

with α. This means that at these higher temperatures, the CH₄ decomposition reaction is further from chemical equilibrium, and can therefore become faster, causing more C* to be formed, which can explain the presence of C*-poisoning when the temperature surpasses 1325 K.

In addition, we can see in Fig. S2d that between around 740 K and 1320 K, β is also lower than the equilibrium constant for CO disproportionation. Therefore, at these middle temperatures, both reactions can cause some C* to form, which can lead to a deviation from the chemical equilibrium compositions shown in Fig. 2 and Fig. S1, because solid carbon is not included in these chemical equilibrium calculations. While this deviation is not visible in the modelling results, it could be present in the experiments, even though it is not reported in Ref. [10], which could explain the higher-than-chemical-equilibrium conversions and yields seen there.

S2.1.2 Paper 2

(a) DRM

In Fig. S3, we present the concentrations that are not shown in the main paper for the comparison between the experiments and model for DRM. The conclusions are similar to what is discussed in the main paper, namely (i) the trends are the same for the experiments and the model, but the modelling results have been shifted to a higher temperature due to the difference in reaction enthalpy for DRM, (ii) the concentration of CO₂ increases and that of the two products decreases around 1280 K due to C*-poisoning, but decreases/increases again when C* is converted by the ER reverse Boudouard reaction, and (iii) the concentrations decrease/increase less rapidly in the model compared to the experiments at higher temperatures, which might also be related to C* formation on the Ni surface.

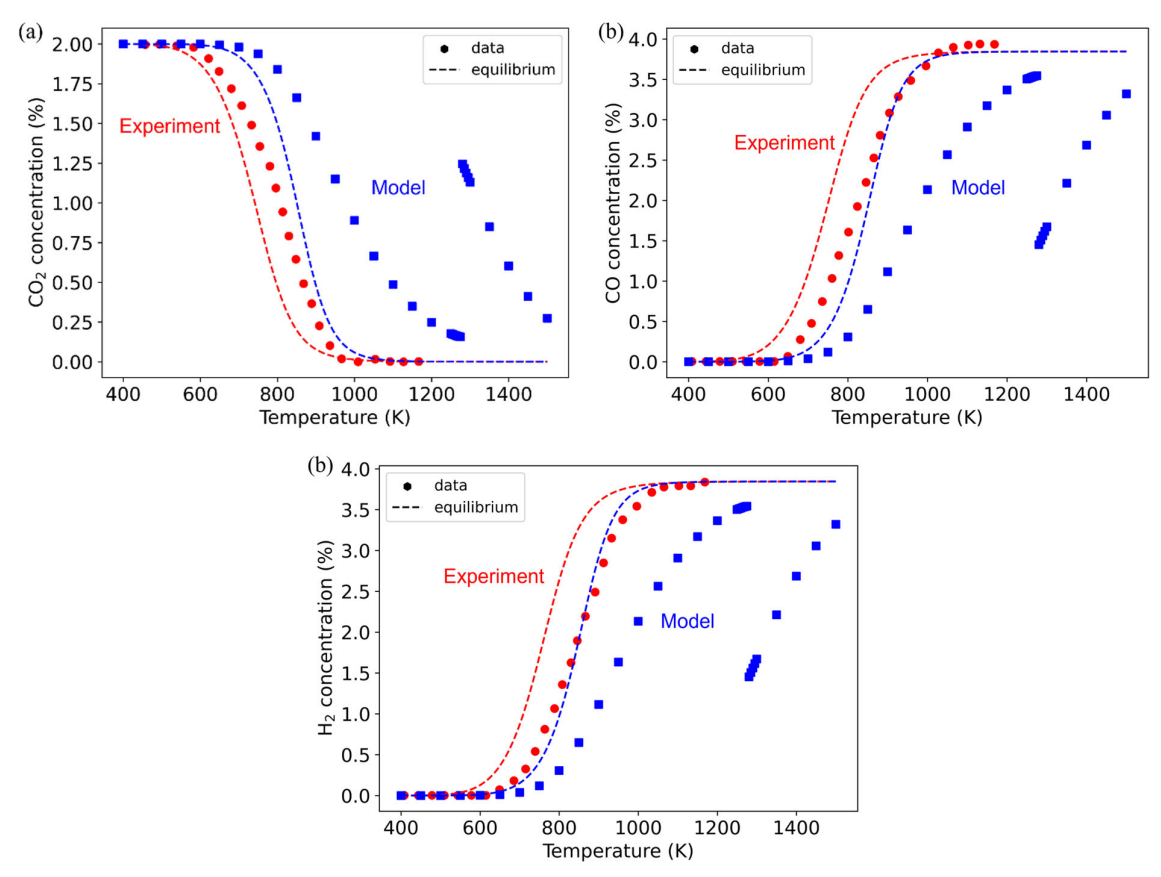


Figure S3: (a) CO₂, (b) CO and (c) H₂ concentration as a function of temperature for the experiments in Ref. [11] (red circles), the modelling results (blue squares) and the corresponding chemical equilibrium compositions for the experiments and modelling results (red and blue dashed lines, respectively). A finer temperature interval of 5 K is used around the transition point between 1250 K and 1300 K to rule out numerical artefacts in the model.

Although the C*-poisoning analysis based on the coverages and rates is discussed in the next section (S2.1.2(b)), similar to the analysis carried out for Paper 1, we can again calculate the α - and β -parameter and compare them to the equilibrium constants for CH₄ decomposition and CO disproportionation. The resulting graphs are shown in Fig. S4.

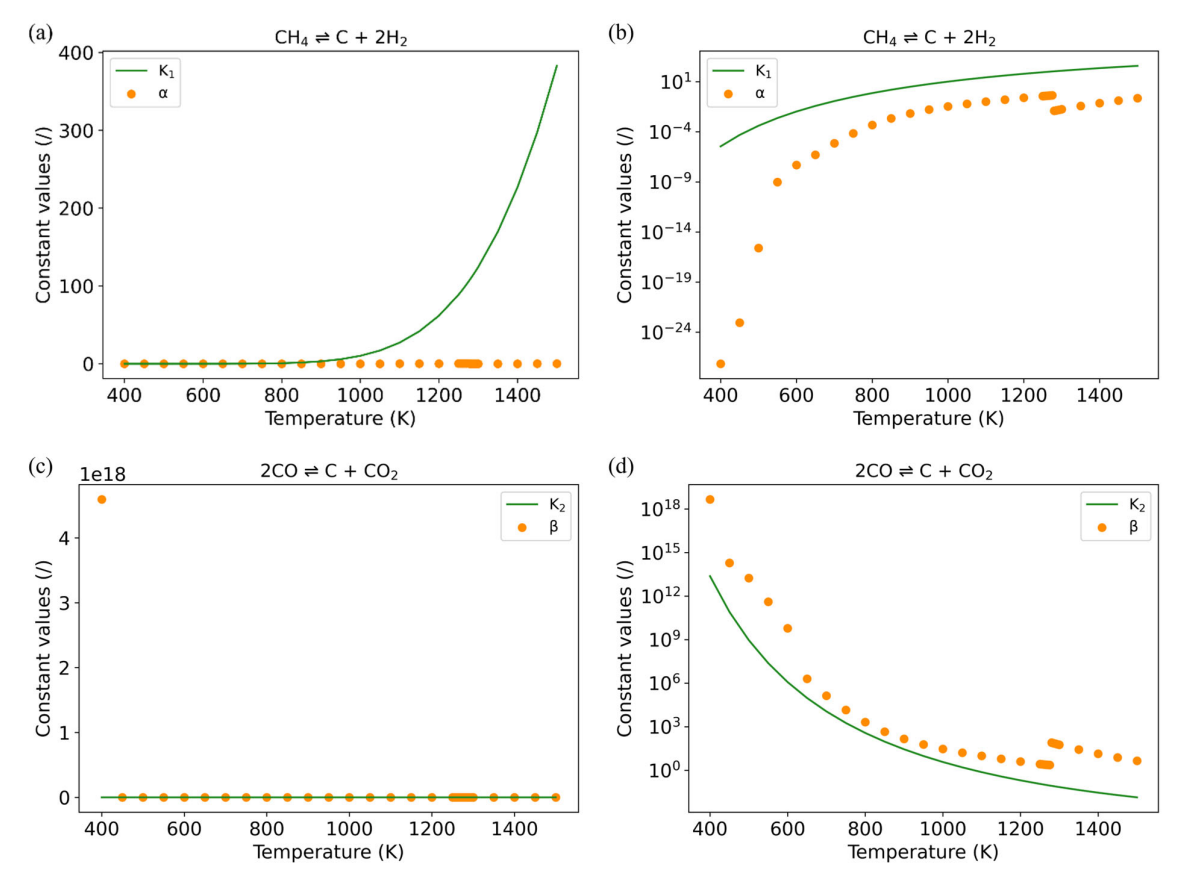


Figure S4: (a, b) α -parameter and corresponding equilibrium constant values as a function of temperature for CH₄ decomposition, both with (a) linear and (b) logarithmic y-scale. (c, d) β -parameter and corresponding equilibrium constant values as a function of temperature for CO disproportionation, both with (c) linear and (d) logarithmic y-scale for Paper 2. When the equilibrium constant values (green lines) are higher than the parameter values (orange dots) the reaction towards the right-hand side of reactions S R.1 and S R.2 will be promoted, causing carbon deposition. A finer temperature interval of 5 K is used around the transition point between 1250 K and 1300 K to rule out numerical artefacts in the model.

As can be seen, these plots have relatively similar trends as in Fig. S2. α remains below K_1 at every temperature, which means that it is thermodynamically favourable to form larger concentrations of C^* and H_2 through this reaction, but especially at higher temperatures this difference becomes much larger, causing the C^* -poisoning seen in the concentration plots (Fig 3 in the main paper and Fig. S3 in the SI). For CO disproportionation, on the other hand, the value of β never decreases below the equilibrium curve, in contrast to Paper 1. This means that at steady state it is thermodynamically not favourable for CO disproportionation to take place at any temperature in this range. Therefore, this reaction cannot explain the deviation and less steep increase/decrease in concentrations at intermediate temperatures. However, at this temperature interval, around 1000 K and higher, the difference between α and K_1 starts to increase, thermodynamically pushing the reaction to the right-hand side, creating more C^* . This could explain the increasing difference between the modelling results and its chemical equilibrium

concentration, which is not seen in the experiments, where this deviation would take place at lower temperatures.

Finally, in the main paper, a lack of H₂O formation is observed in Fig. 3b. The reason for this could be the difference between the theoretical reaction enthalpy for DRM (and other reactions such as SRM) and the reaction enthalpy calculated from the DFT enthalpy data, which cannot be adjusted, because it has been adopted from Ref. [1]. To probe this possibility, we first checked the consistency of the set, ensuring that the energy to convert one species to another via different pathways yields the same value. This was correct. However, because the surface chemistry set only contains surface reactions, adsorption and desorption reactions, no varying pathways could be determined for the gas-phase species to check their adsorption and desorption energies. As a result, the deviation probably lies in the adsorption and desorption reaction enthalpies, which are further investigated in a sensitivity analysis (see Section S2.1.3).

(b) C*-poisoning in DRM

As mentioned in the main paper for the validation with both sets of experiments, the decrease in conversions and yields between 1320 K and 1325 K in Paper 1 and the steep change in concentrations between 1275 K and 1280 K in Paper 2, can be explained by C*-poisoning, especially on Ni(111) and Ni(110). This is demonstrated in Fig. S5, where the C* coverage is plotted on all facets separately and in total.

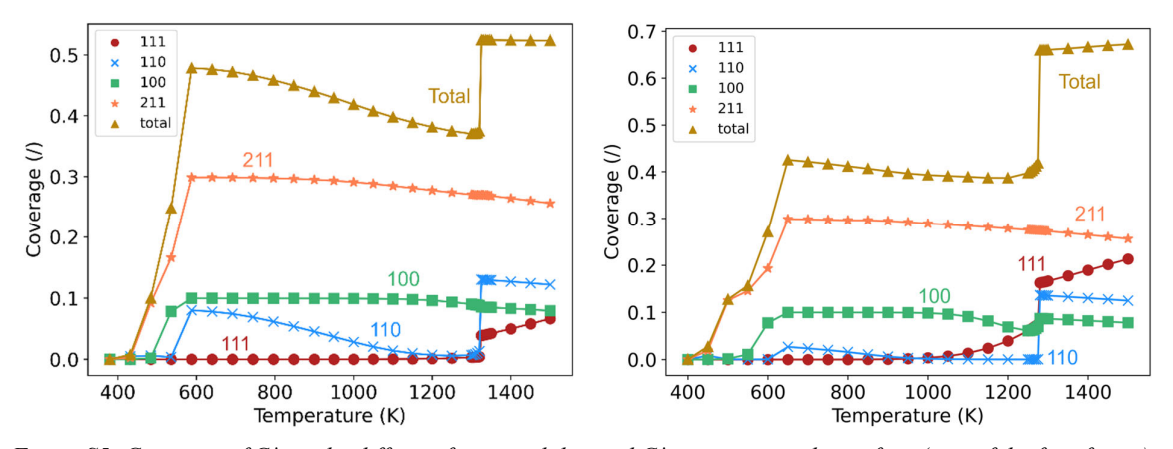


Figure S5: Coverage of C^* on the different facets and the total C^* coverage on the surface (sum of the four facets) as a function of temperature for the input conditions of (a) Ref. [10] (Paper 1) and (b) Ref. [11] (Paper 2).

Around 1320-1325 K in (a) and 1275-1280 K in (b), the C* coverage on Ni(111) and Ni(110) clearly increases. Indeed, for Paper 1, on Ni(110), the most active facet, the C* fraction on the surface increases by 0.117, from 0.013 to 0.130 (the total fraction of Ni(110) is 0.15), while the number of free sites decreases with the same amount from 0.136 to 0.019. A similar drop in the number of free sites on Ni(110) is observed in Paper 2, from 0.149 to 0.014, because the C* coverage increases from 0.0007 to

0.136 from 1275 K to 1280 K. This low fraction of free sites causes the catalyst activity drop and subsequently the sharp decrease in conversion as well.

While this coverage plot explains the causes, it does not explain the sudden change in C^* coverage, which requires an investigation of the reaction kinetics. As shown later in the main paper, in Section 3.2.1, the most important formation reaction of C^* is CH^* dehydrogenation ($CH^* + fs^* \rightleftharpoons C^* + H^*$), and the most important destruction reaction of C^* is C^* oxidation to CO^* ($C^* + O^* \rightleftharpoons CO^* + fs^*$). The net total rates of these reactions at the temperatures right below and above C^* -poisoning are summarized in Table S3.

Table S3: Reaction rates of the most important formation and destruction reaction of C* at 1320 K and 1275 K before C*-poisoning, and at 1325 K and 1280 K with C*-poisoning, for validation Paper 1 and validation Paper 2, respectively. All rates are calculated as the sum of the rates on the four different facets, at the end time of 3600 s.

Danation	Pap	er 1	Paper 2		
Reaction	1320 K	1325 K	1275 K	1280 K	
$CH^* + fs^* \rightleftharpoons C^* + H^*$	0.247 s ⁻¹	0.187 s^{-1}	0.0709 s^{-1}	0.0285 s^{-1}	
$C^* + O^* \rightleftharpoons CO^* + fs^*$	0.238 s ⁻¹	0.0158 s^{-1}	0.0692 s^{-1}	$6.05 \times 10^{-6} \text{ s}^{-1}$	

Below the temperature at which C*-poisoning takes place (1320 K and 1275 K), the C* formation and destruction rates at 3600 s are close to each other, causing them to be approximately balanced. In contrast, at 1325 K and 1280 K, for Paper 1 and Paper 2, respectively, the rates of both reactions have decreased compared to 5 K lower, but especially the rate for C* consumption shows a much larger decrease (up to four orders of magnitude lower than the C* consumption rate at 1275 K and the C* formation rate at 1280 K for Paper 2), indicated in red, which causes a much larger difference between both rates and therefore also results in a much larger net formation of C*, and eventual C*-poisoning.

(c) SRM

The results for the conversion of CH_4 with H_2O are depicted in Fig. S6. At lower temperatures of about 400 K to 700 K, the modelled concentrations do not significantly change, even though some conversion is predicted by the chemical equilibrium concentrations. This is due to the low temperatures, which result in low rates and therefore no appreciable conversion. The same trend can be seen in the experimental results. However, for the experiments, the concentration of CH_4 and H_2O starts to decrease already at lower temperatures, which can be caused by the deviating DFT enthalpy values.

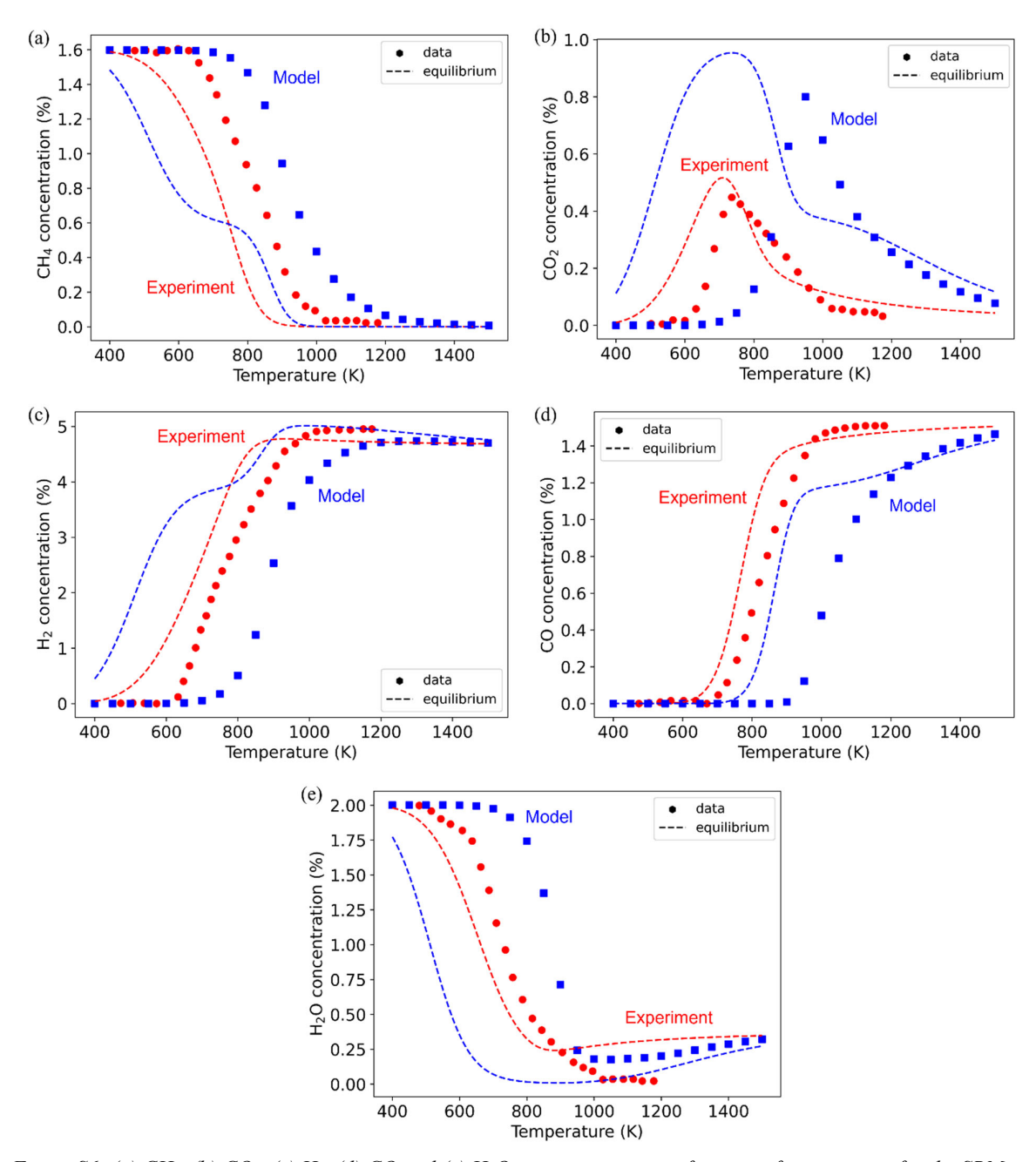


Figure S6: (a) CH_4 , (b) CO_2 , (c) H_2 , (d) CO and (e) H_2O concentration as a function of temperature for the SRM experiments in Ref. [11] (red circles), the modelling results (blue squares) and the corresponding chemical equilibrium compositions for the experiments and modelling results (red and blue dashed lines, respectively).

With increasing temperatures, the calculated results become closer to their chemical equilibrium concentrations, because the reaction rates to reach this chemical equilibrium composition become faster. Although there is a difference between the theoretical and DFT reaction enthalpy calculated chemical equilibrium concentrations for CO₂, CO and H₂O at these higher temperatures above 1000 K, the trends remain the same in the experiments and calculations, and they are only slightly steeper for the modelling results. This difference probably has the same cause as the lack of H₂O formation for DRM, as explained

in the main paper, and is also why we do a sensitivity analysis in Section S2.1.3. In addition to following the same trends, we also see a similar peak in CO₂ concentration, that is located at about 200 K higher temperatures than predicted by the chemical equilibrium composition, similar to the experimental results, although with a larger temperature shift.

In contrast to the DRM results, at the highest temperatures we do not see a sudden increase or decrease in the concentrations caused by C*-poisoning for the simple reason that no C*-poisoning is observed for the SRM results. Indeed, at these temperatures, all concentrations are close to their chemical equilibrium values. The slight overestimation of the CO and H₂O concentration and underestimation of the CO₂ and H₂ concentration are likely due to these gases not having reached chemical equilibrium at the end of the reactor, because the water gas shift (WGS) reaction is not fast enough to convert enough CO and H₂O into CO₂ and H₂. However, overall at these temperatures the calculated concentrations are close to both the theoretical and shifted chemical equilibrium values.

(d) DRM-H₂

In Fig. S7, we show the results for the combined conversion of CO_2 , CH_4 and H_2 . H_2 has been added to the gas mixture to avoid C^* -poisoning, similar to the H_2O addition discussed in the next section. We can again split up the analysis into the low, intermediate and high temperatures. At low temperatures, the experimental and modelling results match, but do not follow the chemical equilibrium concentrations because they are still at their initial conditions and the reaction rates are too slow to cause any conversion. Only for H_2O there is a slight increase in experimental concentrations, but we know that the H_2O formation is underestimated in the model, as explained for DRM. According to the DFT enthalpy based chemical equilibrium, only at the lowest temperatures H_2O would be formed in the model, but in that case the reaction rate is still too low to cause any conversion, and then with increasing temperatures the chemical equilibrium composition quickly drops. Around 500 K - 700 K, we also see a decrease in CO_2 and H_2 concentration in the experiments, which is not present in the model, but this can be explained by the shifted chemical equilibrium compositions. At these temperatures, both the experiments and the model approximately reach their chemical equilibrium concentrations of CO_2 and CO_3 and CO_4 and CO_4

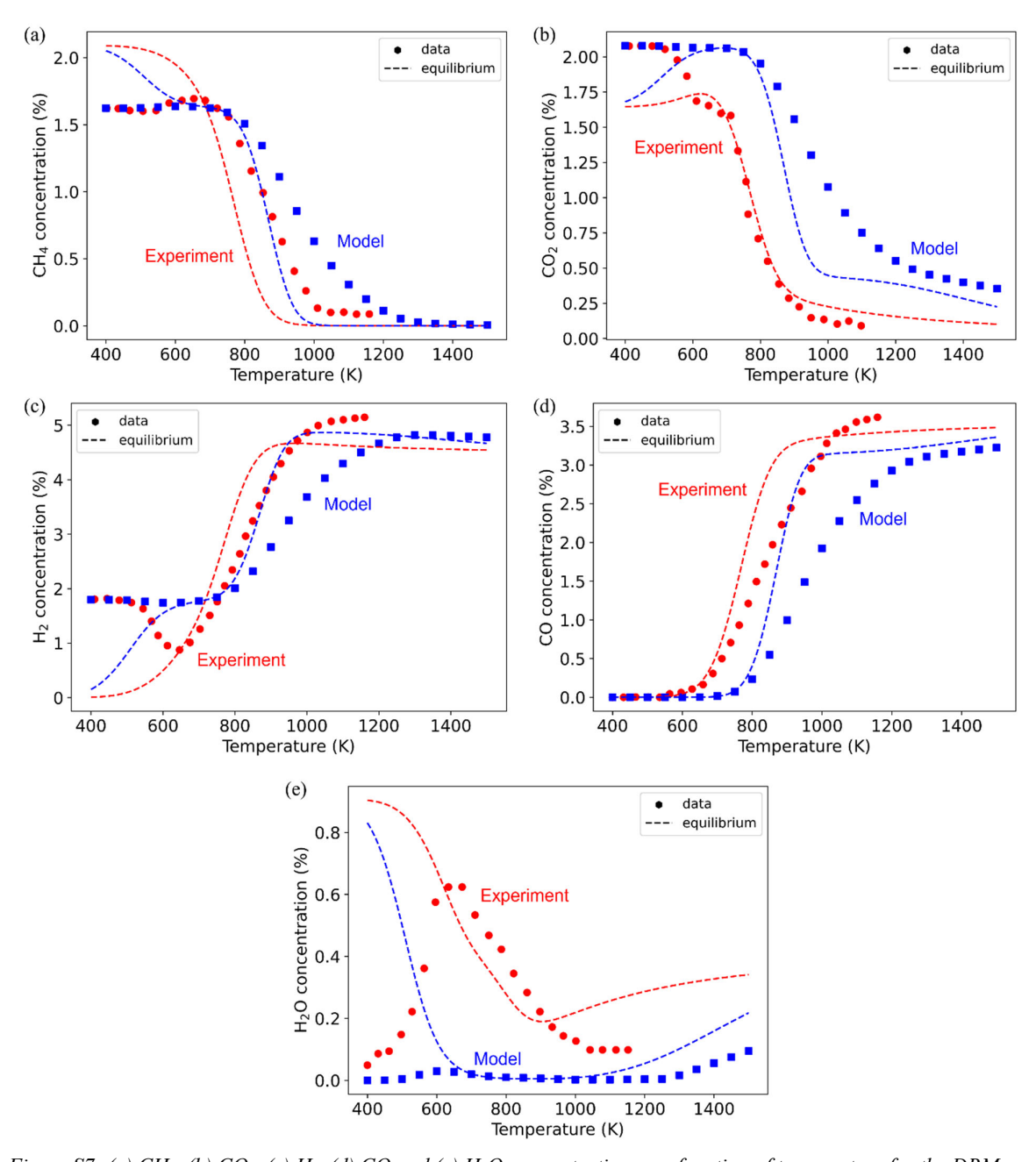


Figure S7: (a) CH_4 , (b) CO_2 , (c) H_2 , (d) CO and (e) H_2O concentration as a function of temperature for the DRM- H_2 experiments in Ref. [11] (red circles), the modelling results (blue squares) and the corresponding chemical equilibrium compositions for the experiments and modelling results (red and blue dashed lines, respectively).

At the intermediate temperatures, we see a similar trend as for the DRM and SRM gas mixtures. The experiments and the model show the same trend, but with a shift to higher temperatures for the model because of the change in reaction enthalpy for DRM (and therefore also DRM + H₂). In addition, we also see that with increasing temperature, the concentration in the calculated results decreases/increases less steeply than in the experiments, which we cannot fully explain because in this case there is no C* being formed on Ni(111) at these temperatures. However, we do see a high C* coverage on Ni(100) and Ni(211), which together make up 40 % of the surface, so this could also be (part of) the explanation.

For the highest temperatures, we again see that the results in the model converge to the chemical equilibrium concentrations, similar to SRM, with some deviations that can be caused by a slower reverse water gas shift (RWGS) reaction, or an overestimated rate of the WGS reaction, which is the opposite of the results found for SRM. This can be explained by the fact that we here add H₂, which promotes the RWGS reaction, while in SRM H₂O is part of the gas mixture, causing the WGS reaction. A slower WGS/RWGS for SRM/DRM-H₂ would lead to a concentration of H₂O/H₂ higher than the chemical equilibrium value, which is indeed what we see in Fig. S6(e)/S7(c).

(e) DRM-H₂O

The results for the CO₂/CH₄/H₂O gas mixture can be found in Fig. S8. We will not discuss them in detail, because these results are similar to the gas mixtures discussed above and in the main paper. Firstly, we again see that the model and experiments start at the same initial conditions and do not react at lower temperatures. Next, at the intermediate temperatures, we see the same trends, but at higher temperatures for the model. Finally, at the highest temperatures, the modelling results are close to the chemical equilibrium concentrations.

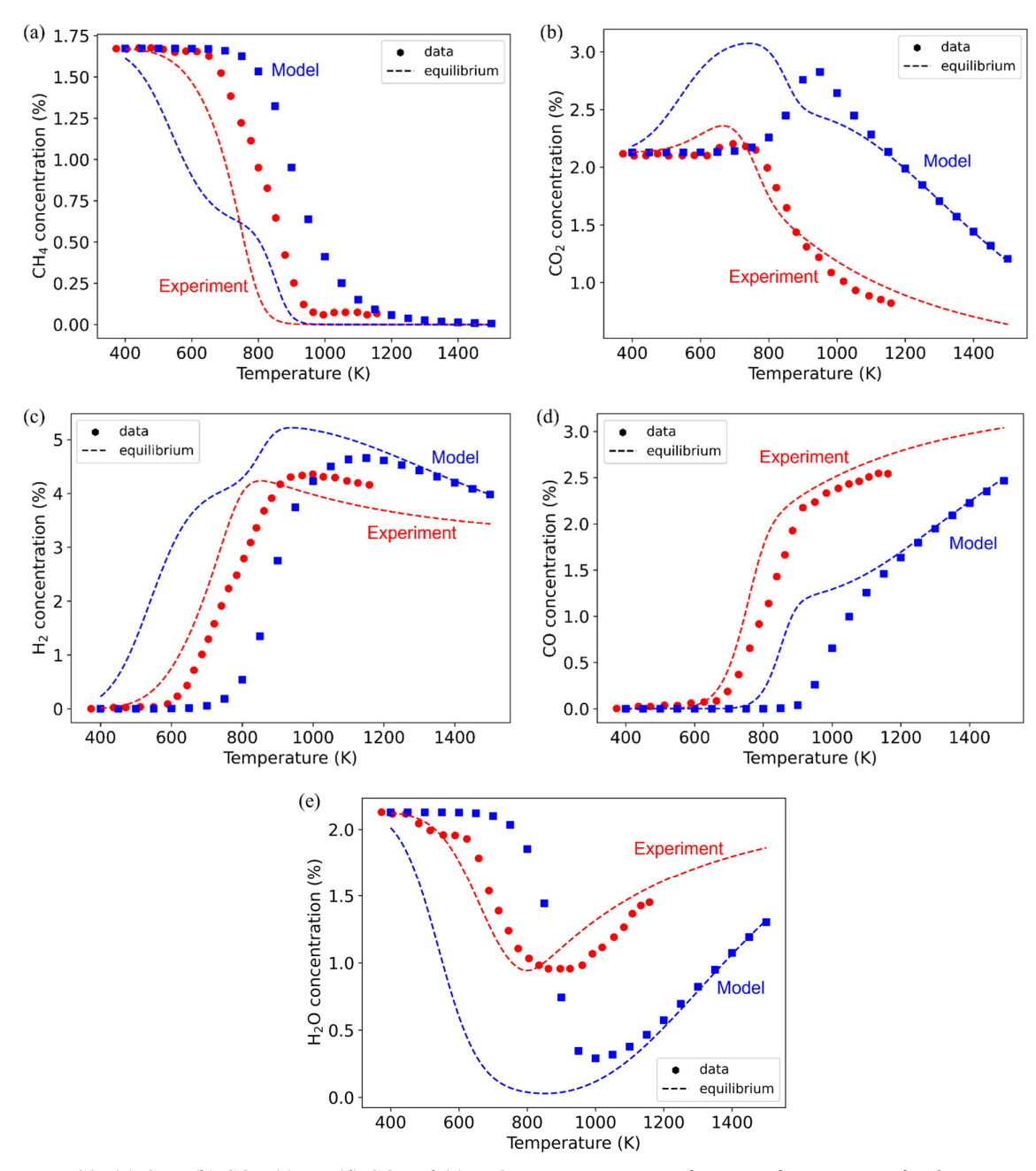


Figure S8: (a) CH_4 , (b) CO_2 , (c) H_2 , (d) CO and (e) H_2O concentration as a function of temperature for the DRM- H_2O experiments in Ref. [11] (red circles), the modelling results (blue squares) and the corresponding chemical equilibrium compositions for the experiments and modelling results (red and blue dashed lines, respectively).

As we can see in Fig. S8, in this case, the chemical equilibrium concentrations based on the experiments and the DFT reaction enthalpies are further away from each other, which might cause deviations in the model. This is because this gas mixture contains a higher H₂O concentration, which is detrimental for the accuracy of our model predictions, as determined and discussed in the main paper. However, in the GAP simulations, we carry out simulations with a gas mixture of only CO₂ and CH₄, without H₂O

addition, so we do not expect this problem. Nevertheless, we should keep in mind when analysing the results that the concentrations of H₂O might deviate from what would experimentally be obtained.

On the other hand, we are able to capture the trends in the experiments with our model. This can especially be noted in Fig. S8 b and e, where the model shows the same maximum in CO₂ concentration and minimum in H₂O concentration, occurring at (slightly) higher temperatures than predicted by the chemical equilibrium concentration, similar to the experiments.

S2.1.3 Sensitivity analysis of the adsorption and desorption enthalpies

For the sensitivity analysis, we performed a literature study and collected papers that report activation barriers and/or reaction energies for the adsorption of CO₂, CH₄, CO, H₂ and H₂O for the four different Ni facets used in our model, which we summarised in the Excel file included as another SI document. The overview tab of this file contains all the data, including some notes on the method and other specifications.

We then separated these data per adsorbed species and facet. For each adsorption reaction of a certain species on a certain facet, we determined a low, mid and high range of both the activation and reaction energy values. For this selection, we applied some criteria:

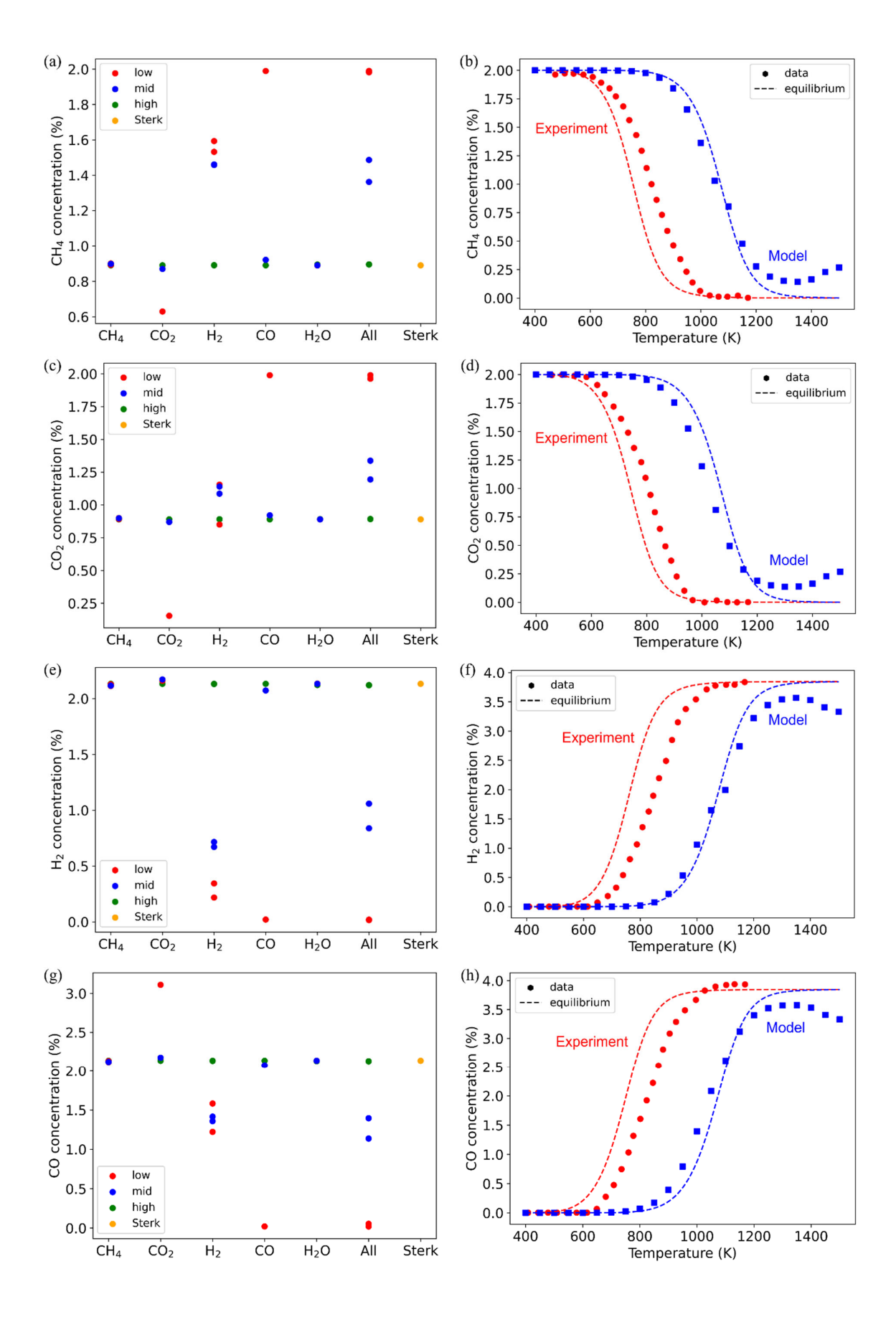
- In case there were many values available, the average was calculated of a defined set of "high", "mid" or "low" values, and a value (from a paper) close to this calculated average was chosen.
- For each adsorption reaction, we always used the activation barrier and reaction energy from
 the same paper, so, where possible, preference was given to papers where both energies had a
 distinct high, mid or low value.
- If no paper exists that has both a high/mid/low activation and reaction energy, we made a separation between both. More specifically, we created an energy set with a, e.g., high activation energy (high-Ea) and the corresponding reaction energy from the same paper, and conversely we created an energy set with a high reaction energy (high-Er) and the corresponding activation energy from the same paper.
- A difference exists between "simple" adsorption reactions and dissociative adsorption reactions. For this, we decided to follow the reactions as reported by Sterk et al. [1], and only selected pure adsorption energies for CO₂, CO and H₂O, and only dissociative energies for CH₄ and H₂.
- For the reaction energies, the sign of the energy value, positive or negative, had to be the same as the values in Sterk et al. [1].
- Some of these sources were not entirely clear on their reported energy data and/or method, thus
 these are indicated in the overview tab by orange or red text (see supplementary Excel file).
 The sources marked in orange were used when no better alternative was available, while the
 sources marked in red were never used

• If the data from Sterk et al. had a distinct high, mid or low value, it was always used for the corresponding adsorption reaction instead of values from other papers

With this method, we tried to select a high, mid and low activation barrier and reaction energy for the adsorption of the five gas species on all four facets. However, we were unable to use some of the collected data once these conditions were applied, and therefore, for some adsorption reactions, not enough data was available or trustworthy enough to define three ranges. In that case, we only worked with the available data, and used the values from Sterk et al. for the missing ranges. In addition, some papers that we chose only reported an activation barrier or reaction energy, but not both. In this case, we also supplied the missing energy, either by the energy from Sterk et al., or by an activation barrier of 0.0 kJ/mol (assuming non-activated adsorption), and separated the range into a range-Ea and range-Er as explained above in criterion 3, when both values were available in separate papers.

In a next step, these energies were inserted into our surface chemistry set, as explained in the Method section of the main paper (Section 2.1.1), by replacing the ΔH_{act} and ΔH_{ads} values obtained from the paper of Sterk et al. [1]. We did this both for every species separately, and for all species simultaneously. For the former, the activation and reaction energy of one species is replaced, to either the low, mid or high range, on all facets, but the energies of the other species are left unchanged, i.e., they retain the values from Sterk et al. For the latter, the energies of all species on all facets are replaced by their low, mid or high ranges. It should be noted, however, that we did not mix these low, mid and high ranges for the different species, using e.g., a low range for one species and a high range for another species, which would lead to an intractable amount of possible energy sets and simulations.

The results of these simulations are shown in Fig. 4 in the main paper, and in Fig. S9, for effect of the different energy sets on the concentrations of the five gas species, and the temperature variation of the concentration of the species for one specific mid energy set. This energy set is named here and in the supplementary Excel file as "All_mid_Er_2", but was renamed to "Mid_Er" in the main paper for simplicity.



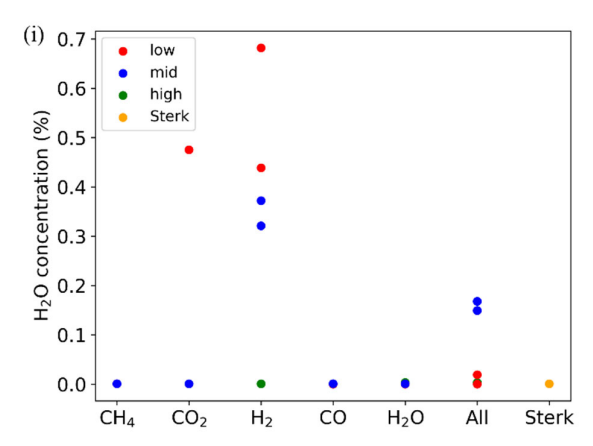


Fig. S9: (a, b) CH_4 , (c, d) CO_2 , (e, f) H_2 , (g, h) CO and (i) H_2O concentration, at 1000 K for all energy sets with low, mid and high energy ranges tested in the sensitivity analysis (a, c, e, g, i) and as a function of temperature for the energy set "All_mid_Er_2" ("Mid_Er") (b, d, f, h). In (a, c, e, g, i), the species on the x-axis indicate the species for which the low, mid and high activation and reaction energy for adsorption are tested, with "All" indicating that all species have their low, mid or high energies tested simultaneously, and "Sterk" reporting the default energy set. In (b, d, f, h) we used one of these "All" energy sets, namely "All_mid_Er_2". The energy values used in each set are given in the Excel file of the SI.

In Fig S9 a, c, e, g and i, we see that the concentrations of the gas species are mostly influenced by the enthalpy values of H₂ adsorption. In addition, the low ranges of CO and/or CO₂ adsorption energy also result in a larger variation in the concentrations. For CO, this can be explained as follows: the values chosen for the low range are calculated using a PW91 or PBE functional. These functionals are known to cause overbinding of CO on Ni [14], which has not been taken into account in these energy values. This can explain their larger effect compared to e.g. the high range for CO, which are the data from Sterk et al., where the energies are corrected for this by adding 40 kJ/mol of destabilisation to CO*.

A second conclusion that we can draw from the plots on the left-hand side is that many concentrations lie close to the orange data point obtained with the energies from Sterk et al.. Therefore, this justifies our use of their surface chemistry energy set, keeping in mind that some deviations are possible, as shown in the effect of the H₂ energies and 'All' energies.

When we compare the left-hand side and right-hand side figures in Fig. S9, the sensitivity analysis overall shows that by using the high, mid or low ranges, a negative effect on the agreement with conversion and product distribution in experiments is achieved, with a higher reactant concentration and a lower product concentration at 1000 K and a general shift of the conversion to higher temperatures.

Two other points we can note from the graphs on the right are (i) at higher temperatures we again see a drop in conversion, which is caused by an increased carbon deposition on Ni(111) and Ni(110), and (ii) the steepness of the increase or decrease in concentration now remains similar to the experimental results, up to around 1200 K, where C* formation is about to start. Therefore, this change in steepness

around 1000 K for the calculated validation results for Paper 2 could partially also be explained by the deviating enthalpy values.

Overall, we used this sensitivity analysis to prove that the lack of H₂O formation is caused by the deviation in surface reaction enthalpy values, and higher H₂O formation can be expected when using other DFT data, but at the cost of creating an inconsistent chemistry set with an even larger shift in temperature for DRM conversion, as can be seen in Fig. S10. Indeed, this larger deviation from the theoretical chemical equilibrium composition is consistently the case for all energy sets that vary the data of all gas species. In addition, the predicted H₂O fraction does not reach the same maximum molar fraction value as the theoretical chemical equilibrium composition. Therefore, we decided to proceed with using the DFT data provided by Sterk et al. [1] for our following GAP simulations.

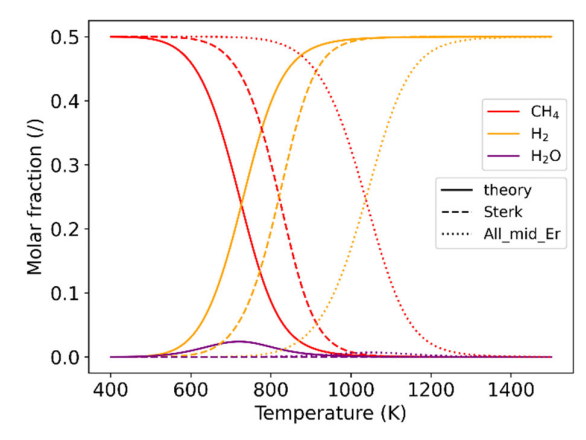


Figure S10: Chemical equilibrium molar fraction of CH_4 (red), H_2 (yellow) and H_2O (purple) as a function of temperature, calculated for the theoretical reaction enthalpies (solid lines), the reaction enthalpies based on the data of Sterk et al. [1] (dashed lines) and the reaction enthalpies from the sensitivity analysis for "All_mid_Er_2" ("Mid_Er") (dotted lines).

S2.1.4 Sensitivity analysis of the lateral interaction energy parameters

As mentioned above, we performed a sensitivity analysis on the lateral interaction energy, in particular the three parameters that define the lateral interactions for C, O and H at θ_{lat} equal to 1, to investigate the influence of our reactant gas mixture (i.e., $CO_2 + CH_4$) on this lateral interaction. The variations in these parameters are taken from Ref. [1], where a similar sensitivity analysis has been carried out, and are given in Table S4.

Table S4: Tested combinations of the lateral interaction energy of C, O and H at $\theta_{lat} = 1$ and their corresponding notation in the plots for the sensitivity analysis of the lateral interaction energy parameters. 0-0-0 corresponds to inclusion of no lateral interactions.

$E_{\theta_{lat}=1}^{C}$	$E_{\theta_{lat}=1}^{O}$	$E_{\theta_{lat}=1}^{H}$	Name
0	0	0	0-0-0
10	10	0	10-10-0
45	45	5	45-45-5
60	60	15	60-60-15
65	75	25	65-75-25
70	70	0	70-70-0
70	70	5	70-70-5
70	75	25	70-75-25
75	75	20	75-75-20
75	75	25	75-75-25
90	90	30	90-90-30

Since we performed the previous sensitivity analysis for the input data of validation Paper 2, we used the same input data here and we run the calculations up to $1200 \, \text{K}$ (avoiding the temperature range where C*-poisoning takes place), using temperature increments of $100 \, \text{K}$ to limit the number of calculations. The results can be found in Fig. S11, which does not include the plot of the H_2O concentration, as the latter has a negligible value over the entire tested temperature range.

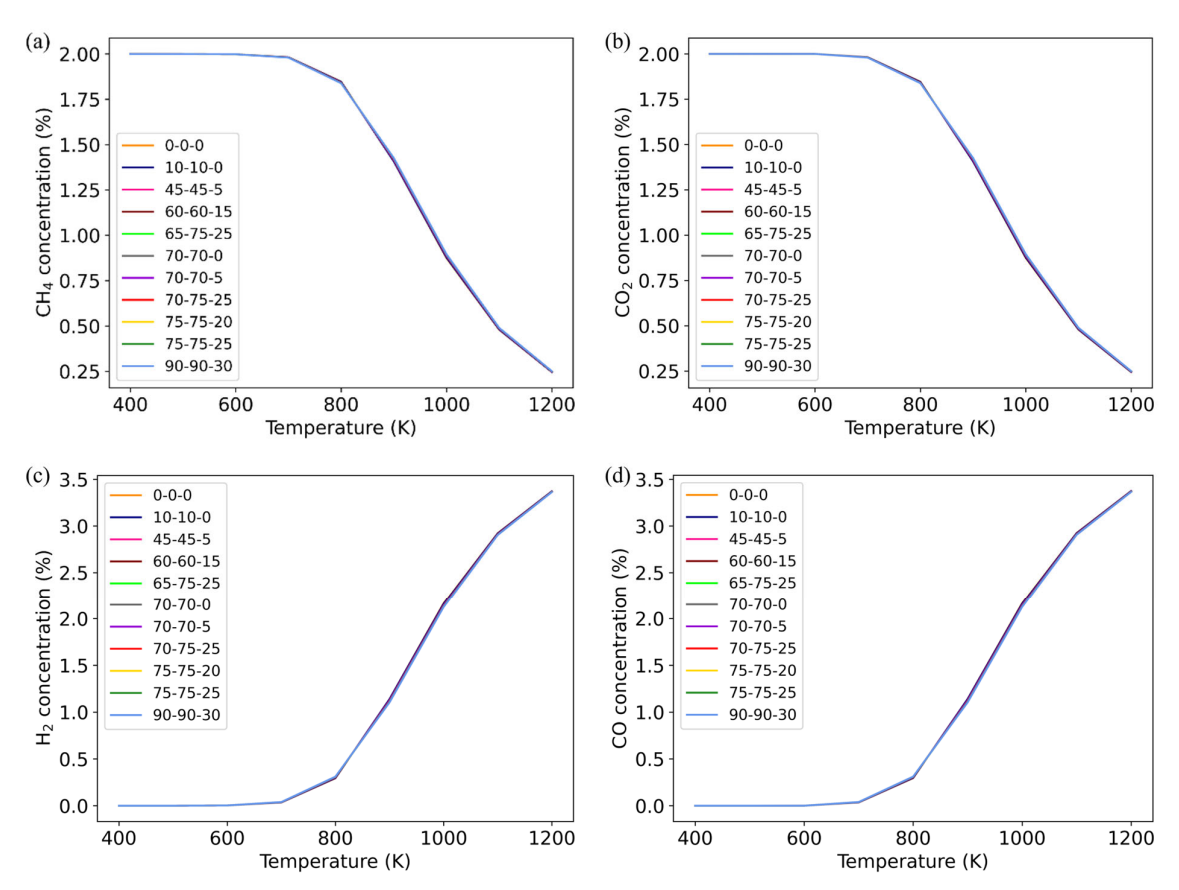


Figure S11: (a) CH_4 , (b) CO_2 , (c) H_2 and (d) CO concentration as a function of temperature for the DRM modelling results based on the input conditions from Ref. [11], at the eleven different combinations of parameters for the lateral interaction presented in Table S4. Note that all curves overlap.

Clearly, the concentrations of the different gas-phase species are equal regardless of the parameters used for the lateral interaction energy. This is similar to what is observed in the sensitivity analysis presented in Ref. [1]. Indeed, the DRM conversion onset in our simulations occurs around 700 K, and at this temperature and above, the results for CO₂ methanation in Ref. [1] also became independent of the lateral interaction parameters used. The only exception found was Ni(100), which in our case is mostly covered by C* and has a lower activity, leading to a negligible influence on the results reported in Fig. S11. Therefore, we can conclude that the inclusion of the lateral interaction energy is not important for our conditions, and the values we chose for the parameters defining this interaction will not influence our results and conclusions.

S2.2 GAP simulations

S2.2.1 Position of the catalyst bed

For the position variation, we made the same plots in Fig. S12 as for the temperature variation presented in Sections 3.2.2(b) and S2.2.4. By comparing these plots to each other, we can see that the values reached at a certain temperature and its corresponding position in the afterglow are similar for all plots, demonstrating the correspondence between temperature and position. Indeed, the results and effect of the catalyst are mostly determined by the gas temperature in the catalyst bed, and less by the length of the afterglow before the catalyst bed or the steepness of the temperature profile between the plasma and the catalyst bed. Therefore, this justifies the use of the different temperature profiles to determine the optimal gas temperature in the catalyst bed and corresponding catalyst position, which should be as high as possible, and therefore as close as possible to the plasma, respectively. The trends observed in the plots of Fig. S12 can be explained in a similar way as the trends in the temperature variation presented in Sections 3.2.2(b) and S.2.2.4. Any small deviations can be explained by the difference in having either a shorter or longer afterglow with the same temperature profile (position variation) or a steeper or less steep temperature profile for the same plasma-catalyst distance (temperature variation), causing some gas-phase species to recombine differently or react further.

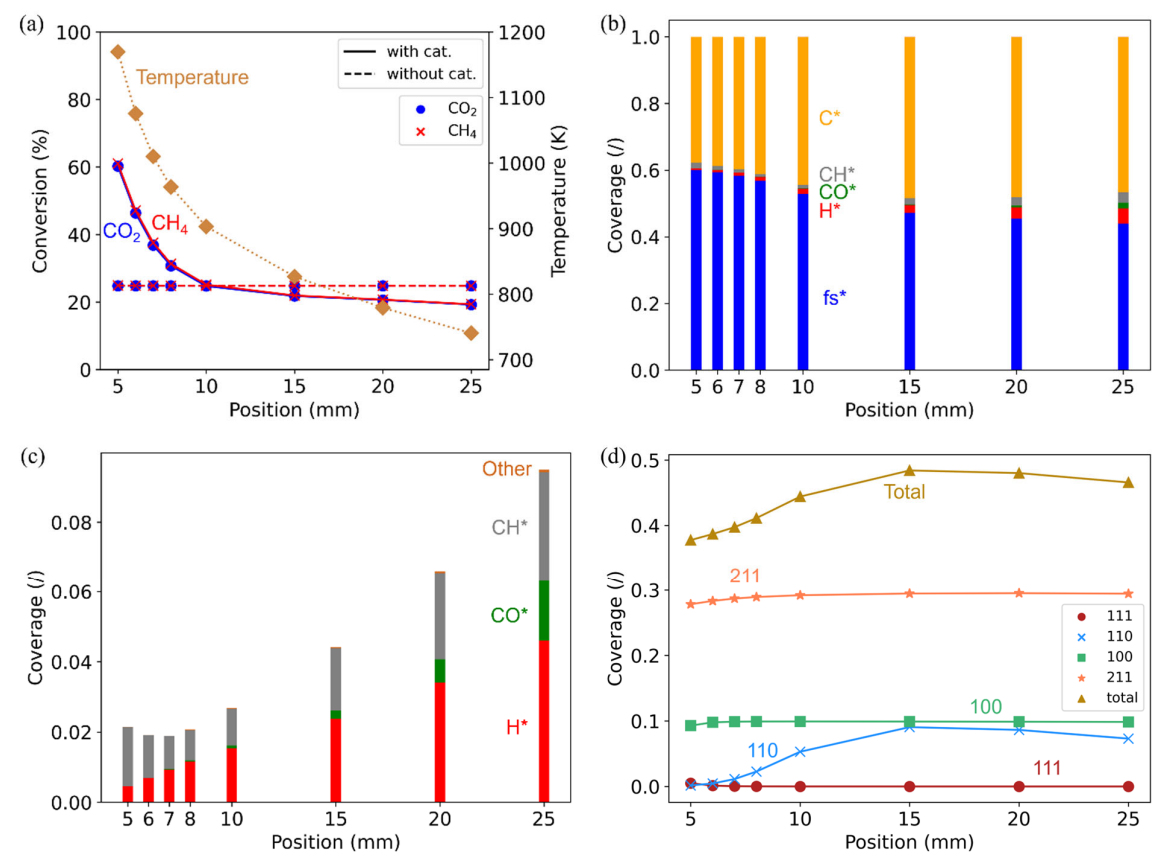


Figure S12: (a) Conversion of CO_2 (blue) and CH_4 (red), both with (solid lines) and without (dashed lines) catalyst, as a function of the catalyst bed position. Note that the CO_2 and CH_4 curves overlap. The gas temperature in the catalyst bed corresponding to each position is shown by a brown dotted line and given on a secondary y-axis. (b) Coverages of the main surface species and the fraction of free sites (fs*) on the surface for each simulated position. (c) Coverages of the surface species that have a coverage lower than 0.1 to make a zoom plot of (b). Coverages lower than 0.0005 are grouped together into "other". (d) Coverage of C* on the different facets and the total C* coverage on the surface (sum of the four facets) as a function of the catalyst bed position.

S2.2.2 Plasma residence time

As mentioned in the Method section (in Section 2.2.2(a)), we also varied the residence time in the plasma, and the effects on the conversions and molar output fractions are illustrated in Fig S13. The results deviate a little below 1 ms, showing an increase in CH₄ conversion and H₂ molar output fraction, and a drop in CO₂ conversion and CO molar output fraction with catalyst, and a drop in both H₂ and CO molar fraction without catalyst, for decreasing plasma residence times. However, all of these metrics converge to an approximately constant value above 1 ms.

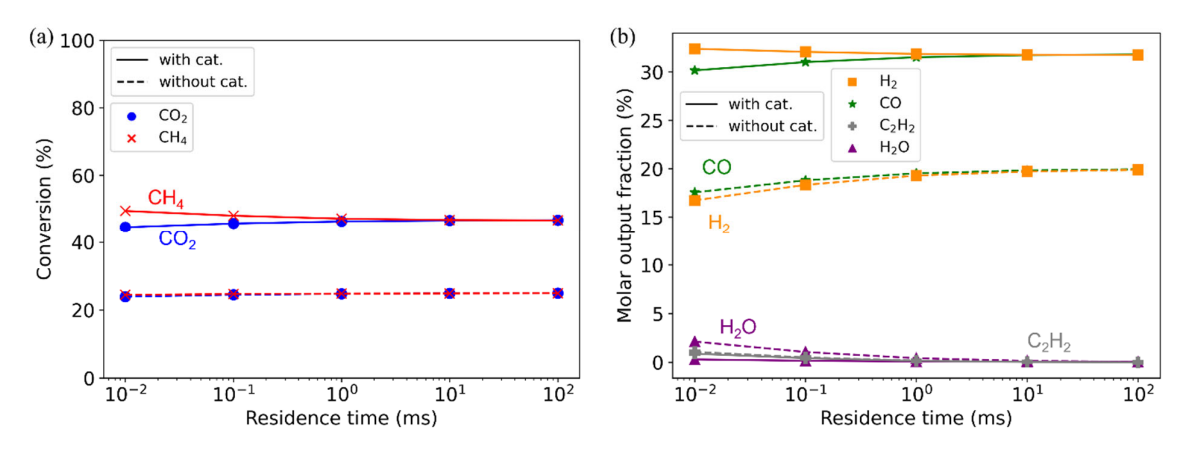


Figure S13: Effect of the plasma residence time on (a) conversion of CO_2 (blue) and CH_4 (red), both with (solid lines) and without (dashed lines) catalyst, and on (b) the molar output fractions of the main products CO, H_2 , H_2O and C_2H_2 . Note that the CO_2 and CH_4 curves in (a) overlap above 1 ms, while in (b) the fractions of C_2H_2 with and without catalyst overlap at all residence times, as well as the CO and H_2 molar output fractions, and H_2O output fractions with and without catalyst above 1 ms.

The difference between CO and H₂ molar output fractions without catalyst can be explained by the formation of H₂O, lowering the H₂ fraction compared to DRM stoichiometry. Upon addition of a catalyst, the water formed at shorter residence times is converted, and this results in an increase in CH₄ conversion and H₂ output, as explained in the reaction mechanism discussion in Section 3.2.1 in the main paper: the H₂O is converted on Ni(111) and slightly on Ni(211), leading to an increase in H* and therefore H₂. In addition, more CH₄ is converted with the O* from H₂O, via CHO* on Ni(111) and via C* on Ni(211). This conversion of C* on Ni(211) also explains the drop in C* on Ni(211) and in general, which we did not include as a plot here.

To explain why H₂O conversion can result in a difference between the CO₂ and CH₄ conversion, and between the CO and H₂ molar fraction, even though the atom balance requires the same amount of CO and H₂ to be formed when only DRM takes place, we can elaborate further on this. In the plasma, part of the CH₄ is converted into C₂H₂, resulting in a lower portion of CH₄ to be converted to H₂O compared to the amount of CO₂ that is converted. As a result, we can have a higher conversion of CH₄ from this H₂O conversion on the catalyst without violating the atom balance, as more CH₄ is still required in the catalyst conversion to have an equal amount of CO₂ and CH₄ converted through H₂O formation into only CO and H₂. So, the increase in CH₄ conversion and H₂ formation is mostly caused by the C₂H₂ formation, but this detour through H₂O is necessary because C₂H₂ can only be formed by the plasma, and the CH₄ conversion in the plasma is limited to 25 %. Another trend that can be noted in Fig. S13b, is the lower CO output fraction with catalyst at low residence times compared to higher residence times, which is caused by the lower CO output fraction without catalyst at these residence times.

Overall, we can conclude that varying the plasma residence leads to some differences that can be explained, especially at shorter residence times, but at 1 ms the results reach more of a constant value,

and therefore the influence of the residence time is quite low. Moreover, in other models, usually a higher (reference) residence time of 10 ms is used, leading to values that are even closer to the stagnated high residence time values [9,15].

S2.2.3 Site density

Fig S14 looks similar to the contribution of every facet to the formation of CO, given in Fig. 6b in the main paper. The trends can also be explained with the same arguments.

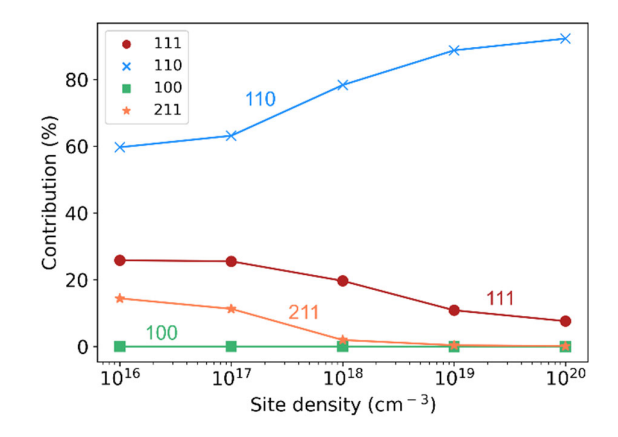


Figure S14: Effect of catalyst site density on the contribution of every facet to the formation of H₂.

S2.2.4 Gas temperature in the catalyst bed

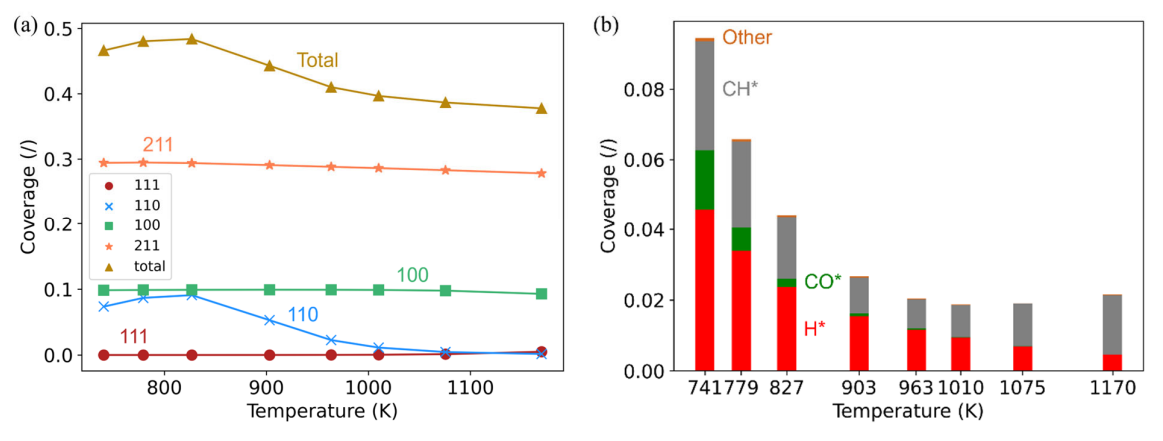


Figure S15: (a) Coverage of C* on the different facets and the total C* coverage on the surface (sum of the four facets) as a function of gas temperature in the catalyst bed. (b) Coverages of the surface species that have a coverage lower than 0.1, to make a zoom plot of Fig. 7b in the main paper. Coverages lower than 0.0005 are grouped together into "other".

S2.2.5 Plasma fraction

Next to the CO and H₂ molar output fractions, in Fig. 8b in the main paper we can also see a small concentration of H₂O at plasma fractions above 25 %, being formed in the plasma (dashed line, without catalyst) and being converted by the catalyst (solid line, lower H₂O output fraction with catalyst). Because this is only a small amount of 0.66 % at a plasma fraction of 45 %, and it may not be visible on

the scale of the graph, we only discuss this here in the SI. At first sight, it would seem that this H₂O conversion on the catalyst can explain the small difference between the CH₄ and CO₂ conversion, and the H₂ and CO molar output fraction. As this H₂O is converted on Ni(111), the CH₄ conversion on this facet is boosted, since more O* species are present on the surface, as explained in the reaction mechanism in Section 3.2.1 (see Fig. 5). This boost in CH₄ conversion is caused by the recombination of CH* from CH₄ with O* from H₂O on Ni(111) to form CHO*, which then dehydrogenates to CO*. With a competing source of O*, the CO₂ conversion is lowered in comparison with that of CH₄. On the other hand, the H₂ production is boosted because the H* from the H₂O decomposition will recombine to form H₂. Therefore, the H₂ can come from both CH₄ dehydrogenation and H₂O splitting on the surface, together creating only one CO molecule, explaining both the gap in the conversion and in the output fractions.

However, overall, the atom balance needs to be retained, and the H_2 and CO (or other reactant or product molecules) required to form H_2O in the plasma will convert back into H_2 and CO on the catalyst, without net changing the product distribution or causing a difference between both product fractions. The latter is only possible when the reaction mechanism is not completed and intermediate species remain on the surface, as for the C^* on Ni(110). Because none of the intermediate species in the reaction mechanism in Fig. 5 are formed in a significant amount on Ni(111) to explain this, we believe that the C^* coverage on Ni(110) is the main cause of the deviation between the CH_4 and CO_2 conversions, and the H_2 and CO molar fractions.

The reaction mechanism remains the same for the different plasma fractions, only changing in the relative contributions of the reactions and facets, such as the H₂O conversion and CHO* formation discussed above.

S2.2.6 Input gas mixture

As mentioned in the main paper, we present here a more elaborate discussion of Fig. 9b and Fig. 10a. The H₂ molar output fraction in the former drops with increasing CO₂ input, without catalyst, but also with catalyst above 30 % CO₂ input fraction. This is logical because H₂ is mainly formed by dehydrogenation of CH₄ (cf. reaction mechanism in Fig. 5 in the main paper), and thus when less CH₄ is present in the input gas mixture, less H₂ will be formed. Without catalyst, this drop becomes steeper above 50 % CO₂, as part of the produced H₂ is converted into H₂O by the excess CO₂. In the presence of a catalyst, a clear improvement in H₂ formation is observed as compared to without catalyst, reaching a peak in H₂ production at 30% CO₂ input fraction. An enhancement below 30 % CO₂ input is observed due to the drop in C*-poisoning, allowing more conversion to take place on the catalyst as a larger proportion of free sites exists, resulting in more H₂ formation from CH₄ conversion. In contrast to the steep drop in the H₂ output fraction without catalyst between 50 % and 70 % CO₂ input fraction, this drop is not as steep with catalyst, and at 70 % CO₂ input fraction, we observe the highest improvement

in H_2 output fraction with catalyst compared to without catalyst, which is caused by the conversion of H_2O , creating more H_2 .

CO production shows a different trend from that of H₂, peaking at 50 % CO₂ and CH₄ input with and without catalyst. Again, we see an improvement in the amount of CO formed when the catalyst is added, except at 10 % CO₂, where conversions are equal due to C*-poisoning of the catalyst. In contrast to H₂, CO is produced both from the dissociation of CO₂* as well as the oxidation of C* from CH₄, as could be deduced from Fig. 5, which relates the formation of CO to both CO₂ and CH₄ conversion. In addition, the highest rates for CO₂ dissociation and CH₄ dehydrogenation on the surface are reached at 30 % CO₂ input, which is explained in more detail in Section 3.2.2(d) in the main paper and below. So, a balance exists between the higher rates and the CO formation from the C* from CH₄ at lower CO₂ input, and more CO₂ that can undergo dissociation at higher CO₂ input, reaching a maximum at 50 % CO₂ input

Besides the main products, H_2 and CO, C_2H_2 is also formed at CO_2 input gas fractions below 50 %, i.e., when more CH_4 than CO_2 is present, as explained in Section 3.2.2(d) in the main paper. This product fraction does not change much, because the surface chemistry set that is applied in this model does not include the conversion of C_2H_2 , meaning that it cannot be converted by the catalyst. It decreases slightly in product fraction when a catalyst is added, because more CO and H_2 are formed, leading to a greater gas expansion and a relative lower contribution of C_2H_2 to the total gas mixture.

In Fig. 10a in the main paper, at CO₂ input fractions above 50 %, the O*-related reactions which result in H₂O conversion accelerate, namely the formation of O* from OH* (orange curve) and the further reaction of O* to convert even more H₂O* into OH* (not shown in the figure because of the lower overall reaction rate), that can in turn also react into O*, indicating the occurrence of H₂O conversion. The latter reaction $(H_2O^* + O^* \rightleftharpoons OH^* + OH^*)$ is also not included in Fig. 5 in the forward direction because it does not take place at a significant rate in the default conditions. As mentioned in Section 3.2.1 and indicated in Fig. 5 in the main paper, H₂O conversion happens mostly on Ni(211) and Ni(111), and is somewhat counteracted on Ni(110), where H₂O is formed, but combined over all facets there will be a net destruction of H₂O on the surface. Catalytic H₂O conversion reaches a maximum at 70 % CO₂, as above 50% CO₂ input fractions, more sites on Ni(211) are available for H₂O conversion due to a lower C* coverage. However, at 90% CO₂ input, there is competition between CO₂ and H₂O conversion, as some CO₂ adsorption and dissociation is also detected on the Ni(211) facet. These reactions S R.3 and S R.4 compete with each other, because they both form O*. When more CO₂ is dissociated through reaction S R.3, this shifts the chemical equilibrium of reaction S R.4, resulting in lower H₂O conversion at 90 % CO₂ input compared to 70 %.

$$CO_2^* + fs^* \rightleftharpoons CO^* + O^*$$
 (S R. 3)

$$H_2O^* + fs^* + fs^* \rightleftharpoons OH^* + H^* + fs^* \rightleftharpoons O^* + H^* + H^*$$
 (S R. 4)

This maximum H₂O conversion at 70 % CO₂ input also causes the maximum in the recombination rate of CH* and O* into CHO*, as can be seen in Fig. 10a. Indeed, H₂O splitting results in a higher O* coverage on Ni(111), which boosts the reaction rate, while still enough CH* is present at 70 % CO₂ input for the reaction to proceed.

Before proceeding with the discussion of Fig. 10a, we will first introduce the concept of degree of rate control, which was introduced by Campbell [16] as:

$$X_{RC,i} = \left(\frac{\partial \ln r}{\partial \ln k_i}\right)_{k_{j \neq i}, K_i} \tag{S16}$$

with $X_{RC,i}$ being the degree of rate control of reaction i, which is a unitless value, r is the overall rate for DRM, k_i is the rate coefficient of reaction i and the derivative is calculated keeping the rate coefficients of all other reactions and the equilibrium constant of reaction i constant. Unfortunately, our Python code does not allow to calculate this derivative automatically. Therefore, we made a similar analysis based on this definition, but using larger differences in k_i .

The value of k_i of a specific reaction is multiplied by the factors 9/10 (0.9) and 10/9 (approximately 1.11), while the other rate coefficients are kept constant, except for the reverse reaction rate coefficient, which is multiplied by the same factor to maintain a constant equilibrium constant. To limit the number of necessary simulations, we limited the reactions of which the rate coefficient is varied to the main reaction pathway, i.e., all CH₄ dehydrogenation reactions, the CO₂* dissociation and C* oxidation reactions, and the adsorption/desorption reactions of CH₄, CO₂, H₂ and CO. Simulations are carried out in which the rate coefficient of one of these reactions has been altered, and from their results the overall DRM rate is calculated for each simulation. This rate is calculated as follows:

$$r = \frac{r_{CO_2,dest} + \frac{r_{CO,prod}}{2}}{2} = \frac{\left(fl_{in,CO_2} - fl_{out,CO_2}\right) + \frac{-\left(fl_{in,CO} - fl_{out,CO}\right)}{2}}{2}$$
(S17)

with $r_{CO_2,dest}$ and $r_{CO,prod}$ being the rate of CO₂ destruction and CO production, respectively, and fl_{in,CO_2} , fl_{out,CO_2} , $fl_{in,CO}$ and $fl_{out,CO}$ the inflow rate of CO₂, the outflow rate of CO₂, the inflow rate of CO and the outflow rate of CO, respectively. Inflow and outflow rates are applied in species/s and calculated over the catalyst CSTR (CSTR 7), so not the complete reactor. The rate of CO production is divided by 2, because of the DRM stoichiometry. In addition, for a production rate, the outflow rate has to be subtracted from the inflow rate, which we included by adding a minus sign for clarity and consistency. This equation takes the average of two of the four species involved in the DRM reaction. The rates of CH₄ destruction and H₂ production are not included, because at the conditions with 30 % CO₂, part of the CH₄ will be converted into C₂H₂ and H₂, making these rates unreliable, while the CO₂ and CO rates are only used in DRM (the effect of the production of H₂O is negligible for both 30 % and 50 % CO₂).

Using these rates, for each reaction the logarithm of the rate is plotted as a function of the logarithm of the rate coefficient. More specifically, the x-axis presents the logarithm of the multiplication factor of the rate coefficient, which gives the same results following from Equation S16. The slope of these graphs then corresponds to the approximation of the degree of rate control, which we call the sensitivity coefficient. Because in our case larger step sizes are used than in a derivative, the results are not guaranteed to result in a straight line. We also tested multiplication factors of 0.5 and 2, but found that these five points (0.5, 0.9, 1, 1.11 and 2) did not show a perfect linear dependence. We believe this might be caused by the too large difference in rate coefficients, that does not only affect the reaction rate of one specific reaction, but will cause other reaction mechanisms to become more important as well. Therefore, we did not include 0.5 and 2 in our final results. These results are plotted for 30 % CO₂ in Fig. S16 and for 50 % CO₂ in Fig. S17.

The most important conclusion we can draw from these graphs is the determination of the rate-limiting reactions. Both at 30 % CO₂ and 50 % CO₂, the highest sensitivity coefficient is obtained for the dissociative adsorption of CH₄, with a value (slope) of 0.3840 and 0.5637, respectively. However, our reaction mechanism exists of three branches, CH₄, CO₂ and H₂O conversion, that are interconnected (mostly through O*), but might also lead to multiple rate-limiting steps. This can also be found in the sensitivity analysis of the reaction mechanism. Although the overall rate-limiting step remains CH₄ dissociative adsorption, CO₂* dissociation and C* oxidation to CO* also have non-negligible sensitivity coefficients of 0.0565 and 0.0249 for 30 % CO₂ and 0.0165 and 0.0061 for 50 % CO₂, respectively. Note that, while the sensitivity coefficient of CH₄ dissociative adsorption increases, the sensitivity coefficients of the two reactions involving CO₂ (or O* from CO₂) decrease with increasing CO₂ input. This is logical, because the higher CO₂ fraction increases the rates of the latter two reactions, making them less rate-limiting, while less CH₄ is present in the gas mixture, decreasing the rate of CH₄ dissociative adsorption even further.

In general, we can conclude that the most important reactions that need to be enhanced to improve catalytic activity are $CH_4(g) + fs^* + fs^* = CH_3^* + H^* > CO_2^* + fs^* = CO^* + O^* > C^* + O^* = CO^* + fs^*$ for the conditions tested. Other reactions, including the subsequent dehydrogenation reactions, all have very low sensitivity coefficients. This also explains why some plots do not show a straight line, as the relative tolerance might be too low to resolve these small differences in rate. The same is true for the H_2 associative desorption, which has sensitivity coefficients in the order of 10^{-7} and is therefore not included in the plots. We could not perform a similar analysis for $70 \% CO_2$, because the model became unstable for most variations in the rate coefficients. However, we assume that the trends observed here will hold for $70 \% CO_2$ as well.

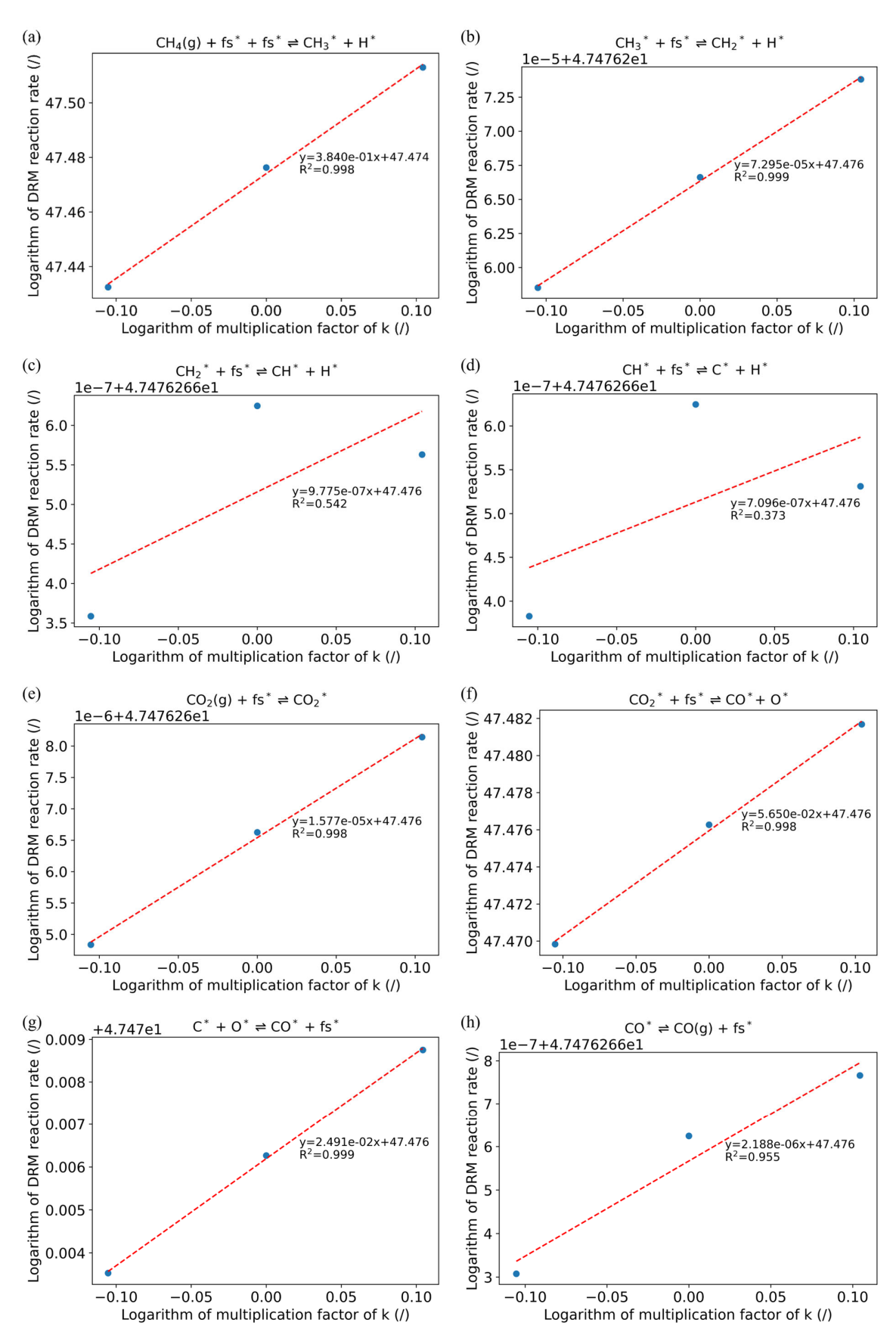


Figure S16: Determination of the sensitivity coefficients at an input gas mixture of 30 % CO2 and 70 % CH4.

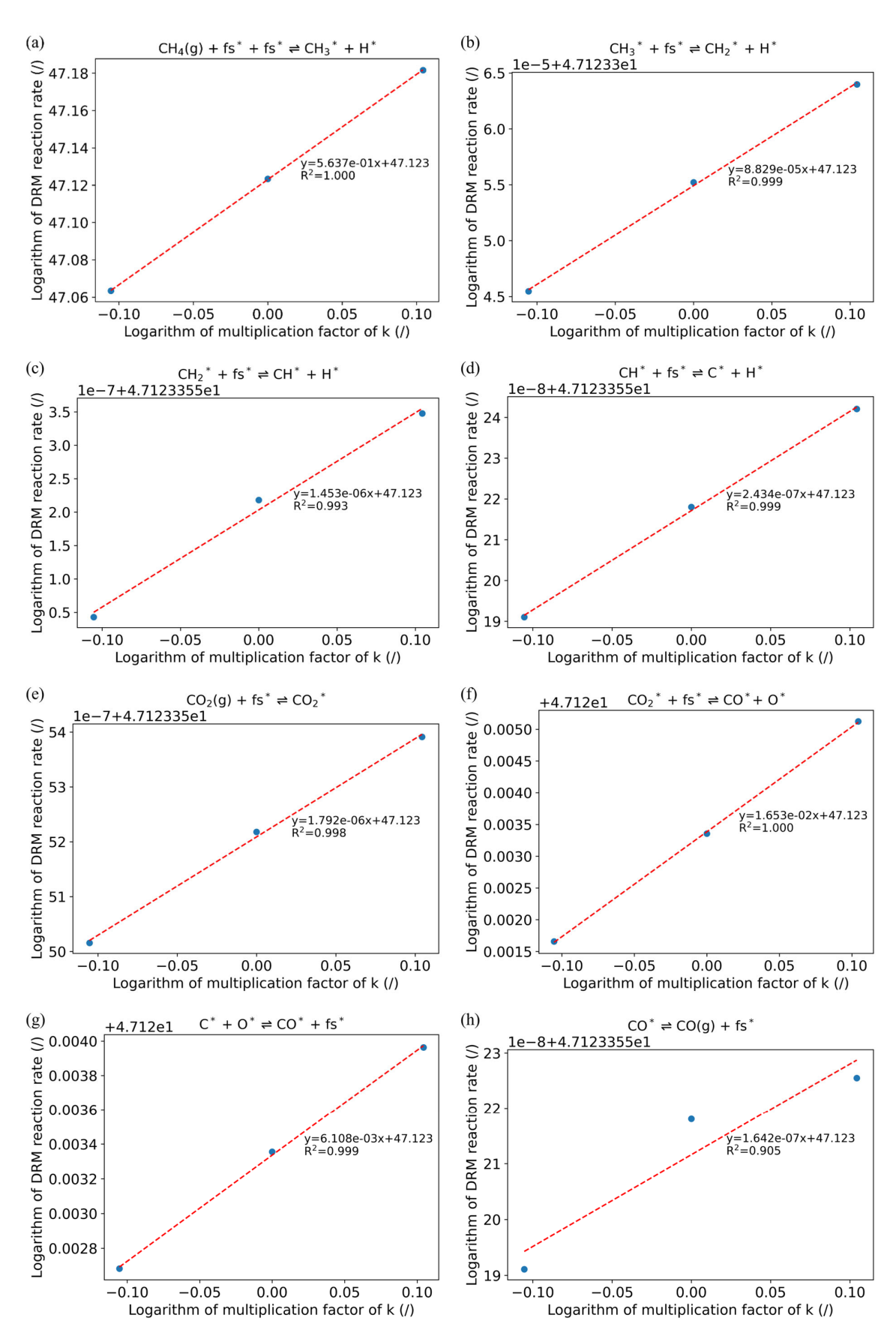


Figure S17: Determination of the sensitivity coefficient at an input gas mixture of 50 % CO2 and 50 % CH4.

Additional insights can be gleaned from Fig 10a, that are also summarized in Section 3.2.2(d) in the main paper. Most importantly, we see that the main production and destruction reactions involving O* are the dissociation of CO₂* and the recombination of O* with C* to form CO*, respectively, as expected from our reaction pathway in Fig. 5. Both reaction rates reach a maximum at 30 % CO2 input, which is reflected in the highest increase in CO production upon catalyst addition compared to without catalyst. Indeed, at higher CO₂ input fractions, the rates of CO₂ conversion (adsorption and dissociation), CH₄ conversion (adsorption and dehydrogenation), and CO formation (CO₂ dissociation, C* and O* recombination and CO* desorption) drop, which contributes to the drop in CO₂ conversion improvement with catalyst, up to the point at 90 % CO₂ input, where only a small improvement in CO₂ conversion is registered. This highlights an important balance in the reaction rates, determined mostly by Ni(110). Reactions that only involve CO₂, such as CO₂ adsorption and dissociation into CO* and O*, reach a maximum at 30 % CO₂, which suggests that the dehydrogenation steps are rate-limiting. Indeed, the CO₂ that adsorbs on the surface can (relatively) immediately react further, form O* and combine with C* from CH₄ dehydrogenation, but the supply of C* through the CH₃* dehydrogenation steps does not become available at the same rate. As a result, at high CH4 input fractions, the rates of the dehydrogenation reactions are enhanced, as are the subsequent reactions involving C* and O*, which in turn also leads to a higher CO₂* dissociation reaction, because O* species will react more promptly with the formed C*. Using the degree of rate control sensitivity analysis discussed above, it is possible to narrow this to one specific dehydrogenation reaction. More specifically, in this analysis, it is demonstrated that this behaviour is caused by the dissociative adsorption of CH₄ being the rate-limiting step, while other dehydrogenation reactions have a significantly lower, practically negligible effect on the overall DRM rate. On the other hand, rate-limiting steps can also be reflected by an increased coverage, and in this case we see an accumulation of C* and CH* in Fig. S18. Similar to the degree of rate control sensitivity analysis, this suggests that multiple rate-limiting steps are present, because both C* and CH* can be oxidised to CO* and CHO*, respectively, indicating the surface oxidation step as another possible rate-limiting step for CO formation. This is also supported by our degree of rate control sensitivity analysis, where C* oxidation is found to be one of the rate-limiting steps. However, the CO₂* dissociation reactions is even more rate-limiting at the investigated conditions, although this is less obvious from our other results, except for the low O* coverage, which should not be the case if only C* oxidation (and CH₄ dissociative adsorption) would be the rate-limiting reaction. Corroborating our results, these observations have been previously reported in literature [17-20]. Indeed, Vogt et al. mentioned CH₄ activation as a rate-limiting step, but also reported that the recombination of C* and O* can be kinetically limiting, with the rate-determining step depending on the input gas mixture [18]. In addition, this paper also assigns CO₂ activation as a kinetically limiting reaction, especially at higher catalyst particle sizes. Because they tested sizes up to 6 nm, and our facet distribution is based on a 8-10 nm particle, this also applies to our simulations, and the work of Vogt et al. in general reports the three same possibly rate-limiting reactions as found in our model [18]. Likewise, Fan et al. investigated

the effect of pressure, and found that at low pressures, CH₄ dissociative adsorption and the oxidation reaction are both rate-limiting, whereas at pressures above atmospheric pressure the oxidation reaction is the only rate-limiting step [19]. Wei and Iglesia, in contrast, only reported the C-H bond activation steps as rate-limiting, without distinguishing which C-H bond breaking reaction is the most rate-limiting, and that the rates are not influenced by the concentration of a co-reactant such as CO₂ [20]. Finally, Wang, et al. deemed CH₄ dissociative adsorption as the rate-determining step, with CHO* as the key intermediate surface species, which is calculated for only a Ni(111) facet [17]. Hence, in relation to the balance mentioned above and in Section 3.2.2(d), while decreasing the CO₂ input gas fraction improves the rates of both CO₂ and CH₄ conversion, as well as CO formation, at CO₂ input fractions equal to or above 30%, these CO2 and CH4 conversion and CO formation rates are lower again at CO2 input fractions below 30 % because the C* coverage starts to become too high, resulting in C*-poisoning. Since this slows down all reaction rates, a balance in CO2 and CH4 input is required to find optimal reaction rates for both CO₂ and CH₄ conversion. On the other hand, at high CO₂ input fractions (e.g. 90 %), the back-reaction of CO* with O* into CO₂* takes place on Ni(100) and Ni(111), counteracting the CO₂ conversion, but these rates are lower than the CO₂ conversion on Ni(110), resulting overall still in a net conversion of CO₂.

We will now continue with discussing the figures in the SI, starting with Fig. S18. In the coverage plots, we can clearly see that more C* and CH* are formed if more CH₄ is present in the input gas mixture. At CO₂ input fractions above 50 %, on the other hand, we see a clear increase in the O* and OH* coverage, related to the conversion of H₂O as discussed above and in Section 3.2.2(d) in the main paper. The coverage of H* can be explained as follows: with increasing CO₂ input, the H* coverage first increases because a larger fraction of the surface becomes available due to the decrease in C*-poisoning and because the dehydrogenation rates are the highest at 30 %; between 30 % and 50 % CO₂ the H* coverage drops because there is less CH₄ present to form H* from and the rates decrease; at 70 % the H* has another maximum because at this ratio the H₂O conversion is the highest, resulting in extra H*.

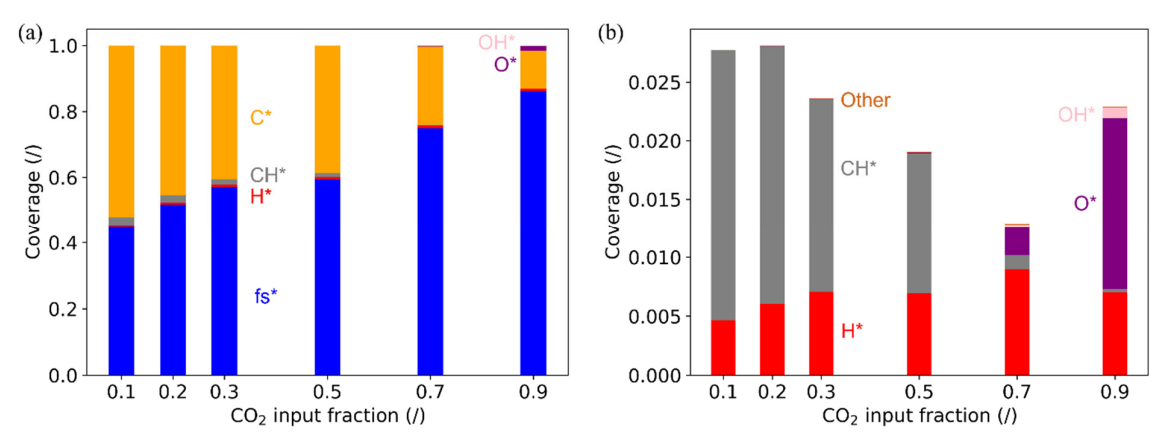


Figure S18: (a) Coverages of the main surface species and the fraction of free sites on the surface, and (b) coverages of the surface species that have a coverage lower than 0.1 to make a zoom plot of (a), for each simulated CO_2 fraction in the input gas. Coverages lower than 0.0005 are grouped together into "other".

The selectivities in Fig. S19 can be related to the same conclusions drawn from the molar output fractions in Fig. 9b and discussed in Section 3.2.2(d) in the main paper and above. The decrease in C_2H_2 selectivity is solely related to the lower contribution of C_2H_2 to the total gas mixture due to the increase in CO and H_2 fraction, because it cannot be converted itself on the catalyst. In the plots, we can also see the clear importance of C_1H_2 conversion to C_2H_2 when the CO_2 input is below 50 %, and the formation of C_2H_2 when the CO_2 input is above 50 %, and its subsequent conversion on the catalyst, lowering its selectivity again. In addition, while some C_2H_4 is formed at 10 % CO_2 input, the formation of C_2H_6 remains negligible at all input gas mixtures.

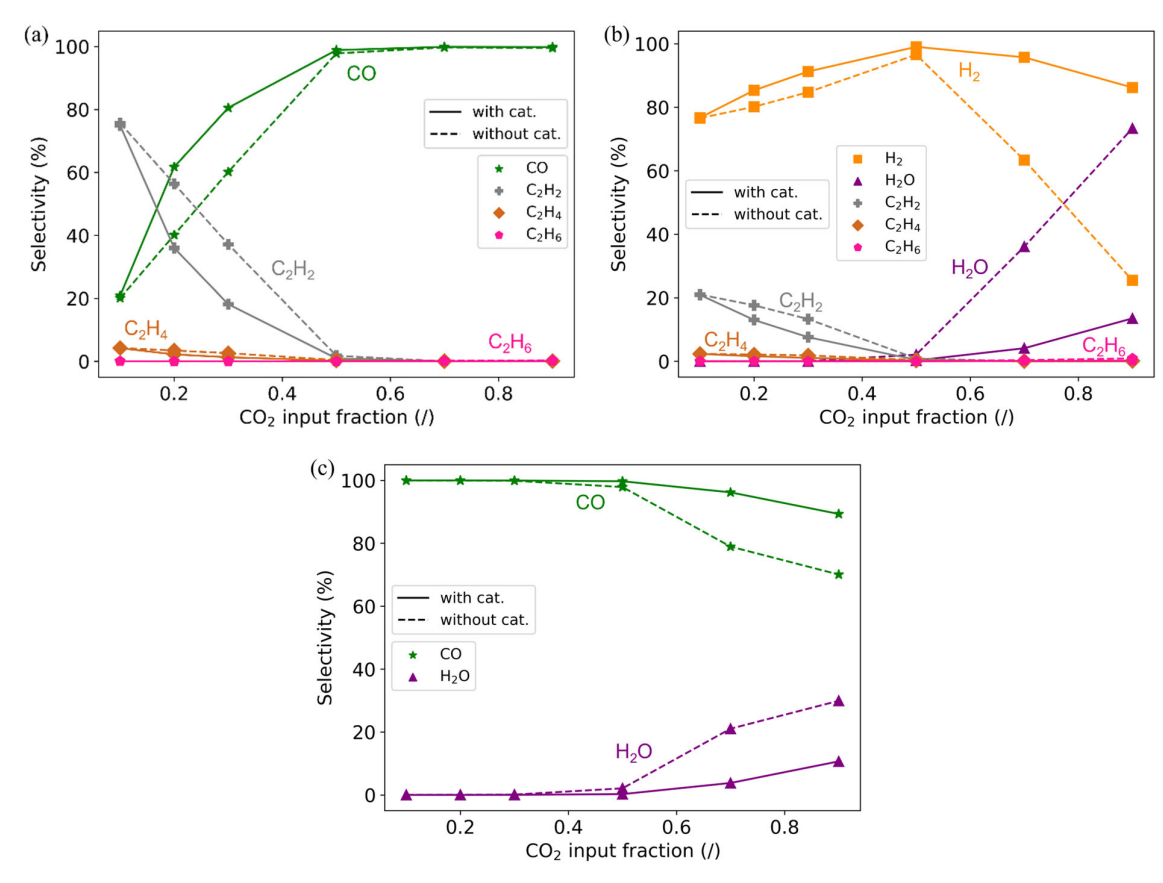


Figure S19: Effect of the CO_2 fraction in the input gas on the selectivities of the most important products, relative to (a) C, (b) H or (c) O, with (solid line) and without (dashed line) catalyst.

As discussed in the main paper, the gas temperature in the catalyst bed and input gas mixture have also been varied simultaneously. The resulting trends will be explained in more detail here.

At a 30/70 CO₂/CH₄ input gas ratio, the rise in CO₂ conversion becomes more steep than at a 50/50 ratio and shifts already towards improving conversion with catalyst below 900 K, around 887 K (compared to 904 K) because a higher CH₄ input fraction leads to higher CO₂ conversion rates. This means that the catalyst can be placed further away from the plasma and still improve the CO₂ conversion. However, this is not the case for CH₄, which keeps its shift at 900 K, so the catalyst cannot be placed too far to avoid a drop in CH₄ conversion. In addition, because more CH₄ is present, the syngas ratio will be above 1 at all temperatures, making the output gas mixture more useful for later applications. This syngas ratio steadily decreases between approximately 2.6 and 1.4 for an increasing temperature from 741 K to 1075 K, with catalyst, and remains practically constant around 1.9 without catalyst. This can again be explained by the higher rates at 30 % CO₂ input: below 900 K the CO reacts faster back into CO₂, increasing the syngas ratio, while above 900 K CO is produced faster, lowering the syngas ratio. Another difference can be found in the output molar fractions: due to the excess of CH₄ in the input gas, some more C₂H₂ is formed. Overall, while this gas mixture is generally better than the 50/50 ratio, and was therefore also briefly described in the main paper, the higher concentration of CH₄ at the inlet enhances

the sensitivity to C*-poisoning, which now takes place at the highest temperature of 1170 K, lowering the conversions and increasing the syngas ratio there.

At a 70/30 CO₂/CH₄ input gas ratio, H₂O conversion is present at all temperatures and plays an important role, changing the conversion and molar output fraction plots. More specifically, for the CO₂ conversion there is a balance between CO₂* being dissociated on Ni(110) above approximately 900 K, and CO* and O* recombination on Ni(111) and Ni(211) up to around 1100 K, caused by the presence of O* from H₂O conversion. Due to this balance, CO₂ only starts to net convert on the catalyst at 980 K, requiring the catalyst to be placed closer to the plasma to yield a positive effect for CO₂. In addition, the CO formation largely follows the CO₂ conversion, and only starts improving between 900 K and 1000 K. If only CH₄ conversion and H₂ production are of interest, the position of the catalyst is less important. Indeed, CH₄ conversion already improves on the catalyst just above 800 K, which is also related to the H₂O conversion, as the O* from H₂O can be used to oxidise C* and CH*, pushing the CH₄ conversion in the forward direction. In addition, the H₂ molar output fraction is always higher with catalyst than without catalyst, even at the lowest temperature of 741 K, which is clearly different from the 50% CO₂ fraction in the input gas mixture described in Section 3.2.2(b), and can again be explained by the H₂O conversion, leading to some extra H*, and the subsequent improvement in CH₄ conversion. Another positive effect is that, with more CO₂ in the inlet gas, no C*-poisoning is observed. However, the syngas ratios become less useful for practical applications, as they do not exceed 1, but increase over the complete temperature range, between 0.5 at 741 K and almost 1 at 1170 K.

When varying the gas composition at higher and lower temperatures, the importance of controlling this temperature is confirmed again. Indeed, at 741 K, the CO₂ and CH₄ conversions decrease with catalyst compared to without catalyst, due to back-reactions happening on the catalyst. The extent to which the conversion decreases depends on the concentration of the species in the input gas mixture: as a general trend, the lower the species is present in the input gas mixture, the larger their drop in absolute conversion. In addition, this also depends on the net rates of CO₂ and CH₄ conversion, which, again reach a maximum at 30 % CO₂ input, similar to the input gas mixture variation at 1075 K described in Section 3.2.2(d) and above. Therefore, the drop in CH₄ conversion starts to become smaller above 50 % CO₂ input, with almost no loss in CH₄ conversion at 90 % CO₂ input. Overall, no net improvement is observed from adding a catalyst, with two exceptions: (i) the H₂ output increases at CO₂ input fractions above 50 % due to H₂O conversion, mostly on Ni(111), and (ii) the syngas ratio is higher at lower CO₂ input fractions, because of the larger loss in CO compared to H₂, especially at 10 % CO₂ input. However, in general we can say that it is not beneficial to place a catalyst further away from the plasma, reaching a lower gas temperature in the catalyst bed, at any input gas mixture.

On the other hand, higher temperatures such as 1010 K and 1170 K yield similar results to 1075 K, and only a change in the steepness of the trends is observed, with the trends being less or more pronounced at lower or higher temperatures. The most important differences are the C*-poisoning and H₂O

conversion. At 1010 K, less to no C*-poisoning is observed, while at 1170 K, this C*-poisoning has expanded up to 30 % CO₂ input, so below 50 % CO₂, the catalyst has no effect anymore. The H₂O conversion above 50 % CO₂ and especially at 90 % CO₂ is more present at the lower temperature of 1010 K, and less at 1170 K. This affects the CO₂ conversion: at 1010 K, there is barely any CO₂ conversion improvement by the catalyst at a CO₂ input fraction of 90 %, due to full oxidation to CO₂ on Ni(111) and Ni(211). However, at 1170 K, this increase in CO₂ conversion is higher than at 1075 K, which is probably caused by the lower C* coverage on Ni(211). The higher CO₂ conversion at 90 % CO₂ input at 1170 K also has as a result that the syngas ratio decreases slightly.

S3. References

- [1] E.B. Sterk, A.-E. Nieuwelink, M. Monai, J.N. Louwen, E.T.C. Vogt, I.A.W. Filot, B.M. Weckhuysen, Structure Sensitivity of CO2 Conversion over Nickel Metal Nanoparticles Explained by Micro-Kinetics Simulations, JACS Au 2 (2022) 2714–2730. https://doi.org/10.1021/jacsau.2c00430.
- [2] F. Girard-Sahun, O. Biondo, G. Trenchev, G. van Rooij, A. Bogaerts, Carbon bed post-plasma to enhance the CO2 conversion and remove O2 from the product stream, Chem. Eng. J. 442 (2022) 136268. https://doi.org/10.1016/j.cej.2022.136268.
- [3] A. Hjorth Larsen, J. Jørgen Mortensen, J. Blomqvist, I.E. Castelli, R. Christensen, M. Dułak, J. Friis, M.N. Groves, B. Hammer, C. Hargus, E.D. Hermes, P.C. Jennings, P. Bjerre Jensen, J. Kermode, J.R. Kitchin, E. Leonhard Kolsbjerg, J. Kubal, K. Kaasbjerg, S. Lysgaard, J. Bergmann Maronsson, T. Maxson, T. Olsen, L. Pastewka, A. Peterson, C. Rostgaard, J. Schiøtz, O. Schütt, M. Strange, K.S. Thygesen, T. Vegge, L. Vilhelmsen, M. Walter, Z. Zeng, K.W. Jacobsen, The atomic simulation environment—a Python library for working with atoms, J. Phys. Condens. Matter 29 (2017) 273002. https://doi.org/10.1088/1361-648X/aa680e.
- [4] B. Loenders, R. Michiels, A. Bogaerts, Is a catalyst always beneficial in plasma catalysis? Insights from the many physical and chemical interactions, J. Energy Chem. 85 (2023) 501–533. https://doi.org/10.1016/j.jechem.2023.06.016.
- [5] B. Zijlstra, R.J.P. Broos, W. Chen, I.A.W. Filot, E.J.M. Hensen, First-principles based microkinetic modeling of transient kinetics of CO hydrogenation on cobalt catalysts, Catal. Today 342 (2020) 131–141. https://doi.org/10.1016/j.cattod.2019.03.002.
- [6] R.D. Johnson ed., NIST Computational Chemistry Comparison and Benchmark Database NIST Standard Reference Database Number 101, (2022). https://doi.org/10.18434/T47C7Z.
- [7] A. Fernández-Ramos, B.A. Ellingson, R. Meana-Pañeda, J.M.C. Marques, D.G. Truhlar, Symmetry numbers and chemical reaction rates, Theor. Chem. Acc. 118 (2007) 813–826. https://doi.org/10.1007/s00214-007-0328-0.
- [8] I.A.W. Filot, Introduction to microkinetic modeling, Technische Universiteit Eindhoven, Eindhoven, 2022.
- [9] J. Slaets, B. Loenders, A. Bogaerts, Plasma-based dry reforming of CH4: Plasma effects vs. thermal conversion, Fuel 360 (2024) 130650. https://doi.org/10.1016/j.fuel.2023.130650.
- [10] J. Kim, M.S. Abbott, D.B. Go, J.C. Hicks, Enhancing C–H Bond Activation of Methane via Temperature-Controlled, Catalyst–Plasma Interactions, ACS Energy Lett. 1 (2016) 94–99. https://doi.org/10.1021/acsenergylett.6b00051.
- [11] K.H. Delgado, L. Maier, S. Tischer, A. Zellner, H. Stotz, O. Deutschmann, Surface Reaction Kinetics of Steam- and CO2-Reforming as Well as Oxidation of Methane over Nickel-Based Catalysts, Catalysts 5 (2015) 871–904. https://doi.org/10.3390/catal5020871.
- [12] B. Wanten, S. Maerivoet, C. Vantomme, J. Slaets, G. Trenchev, A. Bogaerts, Dry reforming of methane in an atmospheric pressure glow discharge: Confining the plasma to expand the performance, J. CO2 Util. 56 (2022) 101869. https://doi.org/10.1016/j.jcou.2021.101869.
- [13] J.M. Ginsburg, J. Piña, T. El Solh, H.I. de Lasa, Coke Formation over a Nickel Catalyst under Methane Dry Reforming Conditions: Thermodynamic and Kinetic Models, Ind. Eng. Chem. Res. 44 (2005) 4846–4854. https://doi.org/10.1021/ie0496333.
- [14] B. Hammer, L.B. Hansen, J.K. Nørskov, Improved adsorption energetics within density-functional theory using revised Perdew-Burke-Ernzerhof functionals, Phys. Rev. B 59 (1999) 7413–7421. https://doi.org/10.1103/PhysRevB.59.7413.

- [15] J. Slaets, E. Morais, A. Bogaerts, Afterglow quenching in plasma-based dry reforming of methane: a detailed analysis of the post-plasma chemistry via kinetic modelling, RSC Sustain. 3 (2025) 1477–1493. https://doi.org/10.1039/D4SU00676C.
- [16] C.T. Campbell, The Degree of Rate Control: A Powerful Tool for Catalysis Research, ACS Catal. 7 (2017) 2770–2779. https://doi.org/10.1021/acscatal.7b00115.
- [17] S.-G. Wang, X.-Y. Liao, J. Hu, D.-B. Cao, Y.-W. Li, J. Wang, H. Jiao, Kinetic aspect of CO2 reforming of CH4 on Ni(111): A density functional theory calculation, Surf. Sci. 601 (2007) 1271–1284. https://doi.org/10.1016/j.susc.2006.12.059.
- [18] C. Vogt, J. Kranenborg, M. Monai, B.M. Weckhuysen, Structure Sensitivity in Steam and Dry Methane Reforming over Nickel: Activity and Carbon Formation, ACS Catal. 10 (2020) 1428–1438. https://doi.org/10.1021/acscatal.9b04193.
- [19] C. Fan, Y.-A. Zhu, M.-L. Yang, Z.-J. Sui, X.-G. Zhou, D. Chen, Density Functional Theory-Assisted Microkinetic Analysis of Methane Dry Reforming on Ni Catalyst, Ind. Eng. Chem. Res. 54 (2015) 5901–5913. https://doi.org/10.1021/acs.iecr.5b00563.
- [20] J. Wei, E. Iglesia, Isotopic and kinetic assessment of the mechanism of reactions of CH4 with CO2 or H2O to form synthesis gas and carbon on nickel catalysts, J. Catal. 224 (2004) 370–383. https://doi.org/10.1016/j.jcat.2004.02.032.